



# Multi-Vib: Precise Multi-point Vibration Monitoring Using mmWave Radar

192

YANNI YANG, Shandong University, China

HUAFENG XU, QIANYI CHEN, and JIANNONG CAO, The Hong Kong Polytechnic University, China

YANWEN WANG\*, Hunan University, China

Vibration measurement is vital for fault diagnosis of structures (e.g., machines and civil structures). Different structure components undergo distinct vibration patterns, which jointly determine the structure's health condition, thus demanding simultaneous multi-point vibration monitoring. Existing solutions deploy multiple accelerometers along with their power supplies or laser vibrometers on the monitored object to measure multi-point vibration, which is inconvenient and costly. Cameras provide a less expensive solution while heavily relying on good lighting conditions. To overcome these limitations, we propose a cost-effective and passive system, called Multi-Vib, for precise multi-point vibration monitoring. Multi-Vib is implemented using a single mmWave radar to remotely and separately sense the vibration displacement of multiple points via signal reflection. However, simultaneously detecting and monitoring multiple points on a single object is a daunting task. This is because most radar signals are scattered away from vibration points due to their tilted locations and shapes by nature, causing an extremely weak reflected signal to the radar. To solve this issue, we dedicatedly design a physical marker placed on the target point, which can force the direction of the reflected signal towards the radar and significantly increase the reflected signal strength. Another practical issue is that the reflected signal from each point endures interferences and noises from the surroundings. Thus, we develop a series of effective signal processing methods to denoise the signal for accurate vibration frequency and displacement estimation. Extensive experimental results show that the average errors in multi-point vibration frequency and displacement estimation are around 0.16Hz and 14 $\mu$ m, respectively.

CCS Concepts: • Computer systems organization → Sensors and actuators; • Networks → Cyber-physical networks.

Additional Key Words and Phrases: millimeter wave, vibration monitoring, wireless sensing

## ACM Reference Format:

Yanni Yang, Huafeng Xu, Qianyi Chen, Jiannong Cao, and Yanwen Wang. 2022. Multi-Vib: Precise Multi-point Vibration Monitoring Using mmWave Radar. *Proc. ACM Interact. Mob. Wearable Ubiquitous Technol.* 6, 4, Article 192 (December 2022), 26 pages. <https://doi.org/10.1145/3569496>

## 1 INTRODUCTION

Monitoring health conditions for structures, such as machines and civil structures, is pivotal for fault diagnosis, which ensures personal safety and reduces economic loss. Structure collapses have incurred hundreds of thousands of accidents and fatalities every year [7]. Maintenance of machine failure can cost up to 40% of the total production cost in plants [31]. Vibration is a critical indicator and one of the primary inducements of structural anomalies.

\*Yanwen Wang is the corresponding author.

Authors' addresses: [Yanni Yang](mailto:yanniyang@sdu.edu.cn), [yanniyang@sdu.edu.cn](mailto:yanniyang@sdu.edu.cn), Shandong University, Qingdao, Shandong, China; [Huafeng Xu](mailto:19092472g@connect.polyu.hk), [19092472g@connect.polyu.hk](mailto:19092472g@connect.polyu.hk); [Qianyi Chen](mailto:19074424r@connect.polyu.hk), [19074424r@connect.polyu.hk](mailto:19074424r@connect.polyu.hk); [Jiannong Cao](mailto:jiannong.cao@polyu.edu.hk), [jiannong.cao@polyu.edu.hk](mailto:jiannong.cao@polyu.edu.hk), The Hong Kong Polytechnic University, Hong Kong, China; [Yanwen Wang](mailto:wangyw@hnu.edu.cn), [wangyw@hnu.edu.cn](mailto:wangyw@hnu.edu.cn), Hunan University, Changsha, China.

Permission to make digital or hard copies of all or part of this work for personal or classroom use is granted without fee provided that copies are not made or distributed for profit or commercial advantage and that copies bear this notice and the full citation on the first page. Copyrights for components of this work owned by others than ACM must be honored. Abstracting with credit is permitted. To copy otherwise, or republish, to post on servers or to redistribute to lists, requires prior specific permission and/or a fee. Request permissions from [permissions@acm.org](mailto:permissions@acm.org).

© 2022 Association for Computing Machinery.

2474-9567/2022/12-ART192 \$15.00

<https://doi.org/10.1145/3569496>

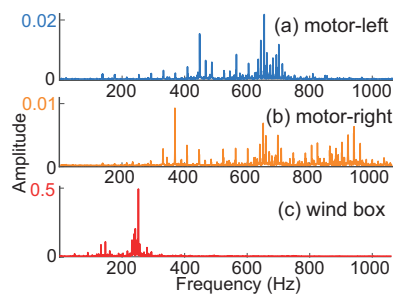


Fig. 1. Spectral patterns of 3 points on the machine in Fig. 2(a): (a) left motor point, (b) right motor point, (c) wind box point

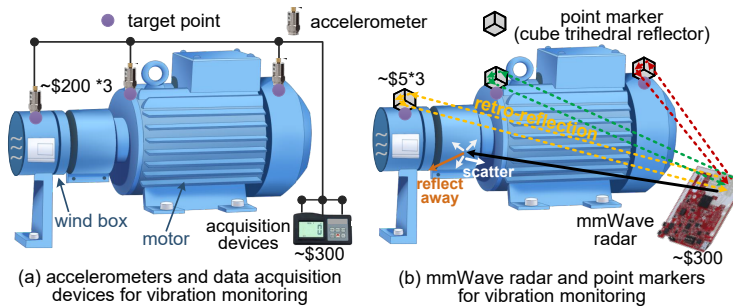


Fig. 2. Comparison of accelerometer-based and mmWave-based multi-point vibration monitoring: (a) accelerometer-based is costly (USD  $\sim 900$ ) and inconvenient, (b) mmWave-based is cost-effective (USD  $\sim 315$ ) and passive.

Research in recent decades has revealed that vibration measurement greatly contributes to the early diagnosis of the damage and impairments in buildings, bridges, and machines [15, 22].

In practice, vibration monitoring is usually carried out at multiple points on the structure since different parts of the structure endure different types of damage and exhibit distinct vibration reactions in terms of vibration frequency and displacement. For example, as shown in Fig. 1, the vibration measured by accelerometers for three points on the blower machine in Fig. 2(a) exhibits different frequency-domain patterns. In a nutshell, the vibration frequency helps infer the type of impairment, and the vibration displacement further indicates how severe the impairment is [25]. For example, the low-frequency and high-amplitude vibration of the wind box in Fig. 1(c) may imply a loose bolt problem in the wind box, while the random and subtle noises residing in the high-frequency band of Fig. 1(a-b) manifest a healthy condition of the motor. Thus, simultaneous vibration measurements at multiple points are essential for precise and holistic fault diagnosis for structures [3, 17].

Existing vibration monitoring solutions can be mainly divided into the following three categories: accelerometer-based, light-based, and radio frequency (RF)-based approaches. Although achieving high accuracy, multiple accelerometers mounted on the structure require in-situ power supplies for data collection, which is cumbersome due to extra installation effort [24, 28]. Instead, light-based (e.g., laser and camera) and RF-based (e.g., RFID and radar) approaches enable battery-free vibration monitoring. However, lasers are expensive (unit price of  $\sim$ USD 1000) for multi-point vibration measurement [20, 21], while cameras are subject to stringent lighting conditions [10, 11]. Recently, RF-based approaches have been widely studied due to their non-intrusive, cost-effective, and light-independent properties. However, existing long-wavelength RF systems (e.g., RFID signal with  $\sim 33\text{cm}$  wavelength) suffer from the limited resolution to accurately measure the tiny vibration displacement [23, 35, 36].

In contrast, the mmWave radar, whose wavelength is within a few millimeters (e.g.,  $\sim 4\text{mm}$  for 77GHz radar), intrinsically provides sufficient resolution for the tiny vibration displacement of structures at *sub-millimeter* levels. As such, the vibration frequency and displacement can be precisely captured from the radar signal reflected from the target structure. However, recent mmWave radar-based systems model the whole structure as *a single vibration point* and intentionally ignore the weak signals reflected by different parts of the monitored structure [13, 19, 29]. Regarding the whole structure as a single vibration source cannot provide sufficient information for precise and simultaneous multi-point vibration monitoring.

In this work, we aim to fill this gap by developing a multi-point vibration monitoring system, called Multi-Vib, using a single commercial mmWave radar ( $\sim$ USD 300). Our intuition is that current commodity mmWave radars potentially offer an opportunity for multi-point vibration monitoring due to its specific design involving (1) the ranging ability achieved by the frequency-modulated continuous-wave (FMCW) chirp signal and (2) the angle-of-arrival (AOA) estimation ability fulfilled by the beamforming technique using the multi-antenna infrastructure. In our work, Multi-Vib is placed in front of the structure with multiple target points to sense the vibration, as

shown in Fig. 2(b). Multi-Vib first sends the radar signal towards the structure. Then, the signals reflected by each point are disengaged from the received superimposed signal using our dedicated signal separation scheme. Finally, Multi-Vib extracts the signal phase from each separated signal in parallel to estimate their vibration frequencies and displacements.

Achieving precise multi-point vibration monitoring using the mmWave radar, however, is not a trivial task. We face two key challenges as follows:

- A fundamental challenge is to simultaneously sense all target vibration points. Intuitively, we can separately detect multiple points at different locations by exploiting the ranging and beamforming ability of mmWave radar. However, our empirical study shows that the signals reflected by points are difficult or even impossible to detect by the radar. This is because most of the incident signal is scattered away by the points to other directions due to their tilted locations and shapes by nature. As shown in Fig. 2(b), the radar signal towards one point of the machine (in solid black) is reflected away (in solid orange) and scattered around (in solid white), resulting in an extremely weak signal back to the radar and missing detection of the point.
- Another major challenge is to precisely measure the vibration displacement. Through our analysis, we find that conventional signal processing methods (i.e., beamforming and null steering) to separate signals and mitigate interferences from multiple vibration points fail to achieve a precise estimation of the sub-millimeter vibration displacement in our scenario (we will explain in detail in Section 4.3). Existing solutions address this issue using the FMCW chirp segmentation technique [19], which, however, decreases the range resolution and impedes accurate measurement of multiple closely located points.

To tackle the issue of weak reflected signal, we conduct systematic analysis of the factors related to signal strength and investigate a new aspect for signal enhancement, i.e., radar cross section (RCS), to mathematically model the signal strength. Through our modeling, our target is to improve the RCS of vibration points. To achieve this goal, we are inspired by the concept of retro-reflectors, which reflect the signal back to its reverse direction with a high RCS and design an effective point marker for signal enhancement. By comparing the RCS performance of different retro-reflectors, for the first time, we introduce the trihedral reflector that enables 3-dimension retro-reflection as our marker for vibration sensing. However, traditional trihedral reflectors only enhance the RCS in a limited range of angles. Thus, we further design an upgraded version to widen the RCS-enhanced angle range. Our experiments show that the designed marker can effectively detect multiple vibration points.

To enable precise estimation of tiny vibration displacement, we design a new and novel method called antenna permutation. Our antenna permutation approach enhances the conventional beamforming and null steering method by fully exploiting the existing multi-antenna design of mmWave radar. In specific, we conduct a comprehensive analysis of the geometric relationship among different antennas, based on which we generate different antenna arrays by delicately permuting all antennas on the radar. Different antenna arrays can introduce multiple and distinctive patterns of signals, which can be integrated together to achieve more precise displacement estimation. Then, beamforming and null steering are conducted for all permuted antenna arrays. By doing so, the signals from different arrays are combined to accurately remove the signal interference, which enables precision extraction of the vibration signal phase and corresponding displacement. Note that our solution maintains the range resolution of the system since we do not modify the FMCW chirp signal.

The novel design of vibration point marker and signal phase refinement method enables a *cost-effective, passive, and precise* vibration monitoring system. First, as depicted in Fig. 2, the mmWave radar and point markers (USD ~315) can greatly save the hardware cost compared with existing accelerometer-based systems for multi-point vibration monitoring (USD 900). Second, our designed point marker can passively reflect the radar signal without extra power supplies. Finally, the combination of the classical null steering beamforming method and our proposed antenna permutation scheme ensures precise measurement of vibration frequency and displacement.

In sum, the main contributions of our work are summarized as follows:

- We propose Multi-Vib, which, to the best of our knowledge, is the first work that employs the commercial mmWave radar for cost-effective, passive, and precise multi-point vibration monitoring.
- We analyze the root causes of the poor performance when applying conventional ranging and beamforming methods for vibration monitoring. Then, we dedicatedly design a retro-reflective marker for accurate point detection and develop effective algorithms to precisely estimate the vibration displacement and frequency.
- We implement Multi-Vib to evaluate the performance of vibration measurement on different real-world machines and civil structures. Experiment results show that the average errors in multi-point vibration frequency and displacement estimation are around  $0.16\text{Hz}$  and  $14\mu\text{m}$ , respectively.

The rest of paper is organized as follows. Section 2 introduces the preliminary knowledge, theoretical modeling, and feasibility study of using the mmWave signal for multi-point vibration monitoring. In Section 3, we introduce our design of the point marker to enable multi-point monitoring. Section 4 presents the implementation details to precisely extract each point's vibration frequency and displacement using the mmWave radar and markers. Then, we evaluate the performance of our system with extensive experiments in Section 5. Next, we introduce related works in vibration monitoring in Section 6 and discuss practical issues and future work in Section 7. Finally, we conclude our work in Section 8.

## 2 MODELING THE MMWAVE RADAR SIGNAL FOR VIBRATION MONITORING

In this section, we first introduce the preliminary knowledge of mmWave radar and analyze how the signals are affected by the vibrating object. Then, we discuss the limitations of the conventional beamforming scheme for multi-point vibration monitoring.

### 2.1 The Principle of Vibration Monitoring with mmWave Radar

The key principle of using the mmWave radar signal for vibration monitoring is that the vibration displacement can be extracted from the signal phase. As shown in Fig. 3(a), a vibration displacement of  $\Delta d$  along the X-axis results in a signal propagation distance change of  $2\Delta d$ . Accordingly, the signal phase change  $\Delta\varphi$  caused by the vibration is  $\Delta\varphi = 2\pi \cdot \frac{2\Delta d}{\lambda}$ , where  $\lambda$  is the signal wavelength.

The phase change  $\Delta\varphi$  can effectively reveal the vibration displacement  $\Delta d$  for the vibration direction perpendicular to the antenna panel, i.e., X axis in Fig. 3(a). For instance, for the 77GHz mmWave signal with  $\lambda = 3.89\text{mm}$ ,

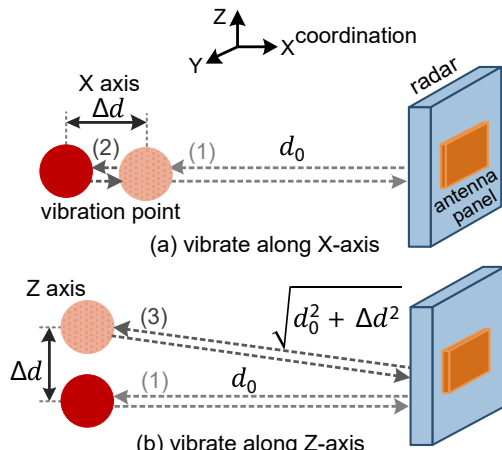


Fig. 3. Modeling of effect of vibration point on signal propagation distance: (a) the point vibrates along X-axis, (b) the point vibrates along Z-axis

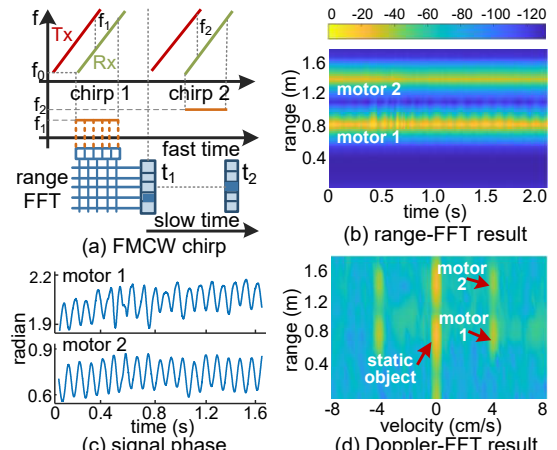


Fig. 4. Illustration of (a) FMCW chirp and range-FFT, (b) range-FFT result of two motors, (c) vibration patterns from signal phase, (d) Doppler-FFT result of two motors

a  $500\mu m$  displacement along the X axis changes a signal phase of  $1.61 rad$ . However, when the vibration direction is parallel to the antenna panel, i.e., Y and Z axes,  $\Delta\phi$  significantly reduces. As shown in Fig. 3(b), for the same  $\Delta d = 500\mu m$  along the Z-axis and  $d_0 = 0.5m$ , the signal propagation distance changes between  $2d_0$  and  $2\sqrt{d_0^2 + \Delta d^2}$ , resulting in  $\Delta\phi = 2\pi \cdot \frac{2\sqrt{d_0^2 + \Delta d^2} - 2d_0}{\lambda} = 1.67 \times 10^{-4} rad$ , which is too small to detect by the radar. Therefore, the mmWave radar is essentially a one-dimension vibration sensor that can measure a point's vibration whose direction is perpendicular to the radar antenna panel.

## 2.2 Extracting mmWave Signal Phase for Vibration Measurement

Existing mmWave radars employ the FMCW chirp signal, whose frequency linearly sweeps over a certain range of frequency band:  $f(t) = f_0 + kt$ , where  $f_0$  and  $k$  are the starting frequency and chirp rate, as shown in Fig. 4(a). A FMCW chirp signal can be expressed as  $x(t) = e^{j(2\pi f_0 t + \pi k t^2)}$ . The radar transmitter (Tx) first sends out the chirp signal, which is then reflected by the vibration point and propagates back to the receiver (Rx) with a time delay of  $\tau = \frac{2(d_0 + \Delta d(t))}{c}$ , where  $c$  is the signal propagation speed. The received signal can be represented as  $y(t) = \alpha \cdot x[t - \tau]$ , where  $\alpha$  is the signal attenuation factor. The intermediate frequency signal can be obtained as [19]:  $s(t) = x^*(t) \cdot y(t) \approx \alpha \cdot e^{j4\pi(f_0+k)t} \cdot \frac{(d_0+\Delta d(t))}{c}$ , where  $(\cdot)^*$  refers to the conjugate operation. Then, fast Fourier transformation (FFT) is performed on  $s(t)$  in each chirp, which is called range-FFT [27]. Each frequency corresponds to a range bin which is the distance between the vibration point and the radar. Finally, we select the complex-value signal in the target range bin  $d_i$  (the bin including  $d_0$ ) from all chirps as  $s_i(t) = \alpha e^{j4\pi f_0(d_i + \frac{2\Delta d(t)}{c})}$  and extract the phase from  $s_i(t)$ .

In Fig. 4(b), we depict the signal amplitude after range-FFT where two motors separately vibrate in different range bins, i.e.,  $0.8m$  and  $1.4m$ . Then, we extract the signal phase from the two target range bins to observe each motor's vibration pattern, as shown in Fig. 4(c). We further measure the vibration velocity by performing a second FFT to obtain the Doppler-FFT spectrum, as shown in Fig. 4(d). Two motors both vibrate with a speed of around  $4cm/s$ . So far, we show that the ranging ability of FMCW chirp signal can help to extract the signal phase of multiple vibration objects located in different range bins. However, for multiple vibration points with compact distance, they may locate in the same range bins. Therefore, merely using the ranging method fails to separately extract multiple points' vibration patterns. To this end, mmWave radar employs the beamforming technique as well as range-FFT to differentiate multiple compact vibration points in both range and angular dimensions.

## 2.3 Beamforming and Its Limitation for Multi-point Vibration Monitoring

Current mmWave radars are equipped with multiple Tx and Rx antennas. In Fig. 5(a), we show the antenna layout of a commercial mmWave radar with 3 Tx antennas (Tx1-3) and 4 Rx (Rx1-4) antennas. The multi-antenna design enables us to separate the signals reflected by multiple points and obtain their AOAs via beamforming.

As shown in Fig. 5(a), with an interval of  $\frac{\lambda}{2}$  between Rx1 and Rx2, the signal transmitted from Tx1 and received by Rx2 will experience an extra propagation distance of  $d_e = \frac{\lambda}{2} \cdot \sin\phi$  than that received by Rx1, where  $\phi$  refers to the AOA. This results in a phase difference of  $\frac{2\pi}{\lambda} \cdot d_e$  between Rx1 and Rx2. Accordingly, phase differences

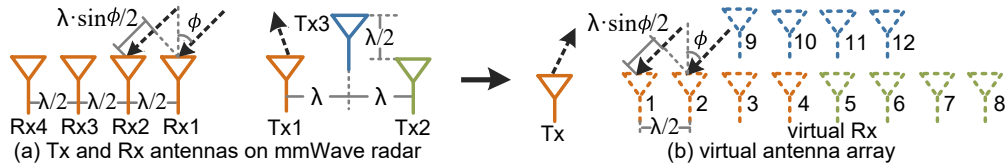


Fig. 5. Antennas on the mmWave radar: (a) physical antenna array with 3 Tx and 4 Rx antennas, (b) virtual antenna array with 1 Tx and 12 Rx antennas

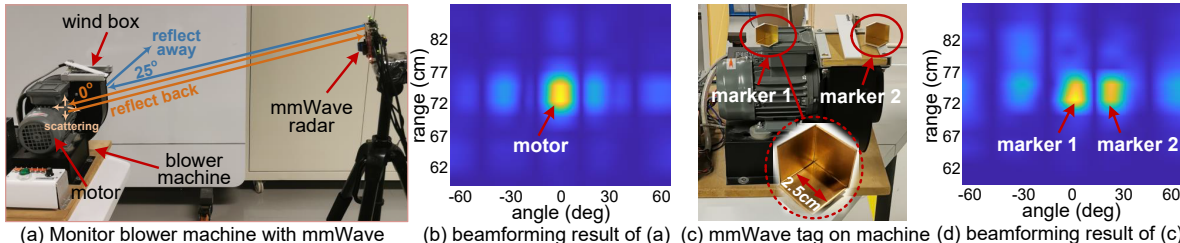


Fig. 6. Beamforming result for monitoring a blower machine with mmWave: (a) monitor blower machine with the mmWave radar, (b) beamforming result of the received signal reflected by the whole machine, (c) attach our designed point markers on the machine, (d) beamforming result of the signal reflected by two markers

between the signal arriving at Rx3/Rx4 and Rx1 are  $\frac{2\pi}{\lambda} \cdot 2d_e$  and  $\frac{2\pi}{\lambda} \cdot 3d_e$ , respectively. Due to another  $2\lambda$  separation between Tx1 and Tx2, phase differences between the signal from Tx2 to Rx1/2/3/4 and that from Tx1 to Rx1 are  $\frac{2\pi}{\lambda} \cdot 4d_e$ ,  $\frac{2\pi}{\lambda} \cdot 5d_e$ ,  $\frac{2\pi}{\lambda} \cdot 6d_e$ , and  $\frac{2\pi}{\lambda} \cdot 7d_e$ , respectively. For simplicity and better understanding, we can transform the physical layout of Tx1, Tx2, and Rx1-4 antennas into a virtual linear antenna array with one Tx and eight Rx antennas, i.e., the linear Rx 1-8 as depicted in Fig. 5(b). Similarly, based on the geographical relationship between Tx3 and Tx1, another four virtual Rx antennas 9-12 are transformed parallel to virtual Rx 1-8 and align with virtual Rx 3-6. Since Rx antennas 3-6 and 9-12 are duplicated along the azimuth dimension, we can simply employ the virtual linear antenna array Rx antennas 1-8 to perform beamforming. Then, the phase difference  $\Delta\varphi_m(\phi)$  between the virtual Rx  $m \in [1, 2, \dots, 7, 8]$  and virtual Rx 1 can be expressed as:

$$\Delta\varphi_m(\phi) = \frac{2\pi}{\lambda} \cdot (m - 1) \cdot d_e = \pi \cdot (m - 1) \cdot \sin\phi \quad (1)$$

Then, a steering vector  $w(m, \phi)$  is formulated based on  $\Delta\varphi_m(\phi)$  as follows:

$$w(m, \phi) = e^{-j\Delta\varphi_m(\phi)} \quad (2)$$

Finally, we multiply the steering vector with the received signal  $s_{i,m}(t)$  after range-FFT on virtual Rx antennas 1-8 and obtain the beamformed signal  $Y(i, \phi, t)$  as below:

$$Y(i, \phi, t) = \sum_{m=1}^8 w(m, \phi) \cdot s_{i,m}(t), \quad (3)$$

where  $i$  and  $m$  denote the index of the range bin and antenna, respectively. In Eq. (3), we sweep  $\phi$  in the range of  $[-90^\circ, 90^\circ]$  with a step of  $1^\circ$ . The amplitude of  $Y$  will peak at  $(i, \phi)$  where a reflector is located.

We apply range-FFT and beamforming to measure the signal reflected by a vibrating blower machine, as shown in Fig. 6(a). The blower machine consists of two components, i.e., the motor and wind box, which bear different impairments and require separate monitoring. However, the signal amplitude after beamforming, as depicted in Fig. 6(b), only exhibits a single target that corresponds to the location of the motor, but fails to detect the wind box. This is because the motor is located vertically to the radar ( $0^\circ$ ) so that part of the reflected signals directly propagate back to the radar (other parts of signal are scattered around due to the motor cylinder shape). Moreover, the motor has a larger area to reflect back the radar signal. However, the smaller wind box located in a tilted direction to the radar ( $25^\circ$ ) with a flat surface reflects most of the radar signal to another direction instead of propagating back to the radar. As such, the reflected signal captured by the radar is extremely weak, resulting in missing detection of the wind box. Therefore, to achieve multi-point vibration monitoring, a fundamental challenge is to increase the signal strength for all target vibration points.

### 3 DESIGN OF THE MARKER FOR MULTI-POINT VIBRATION MONITORING

In this section, we introduce our method to enhance the signal strength of target vibration points, which is achieved by a delicate design of the point marker.

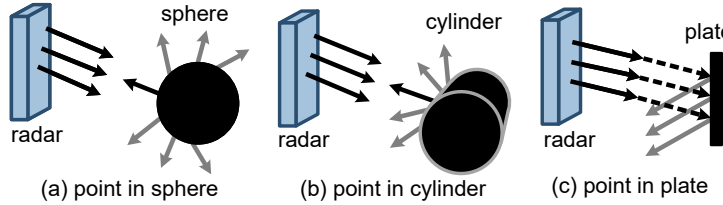


Fig. 7. Tilted location between the mmWave radar and different forms of vibration points: (a) sphere, (b) cylinder, and (d) plate

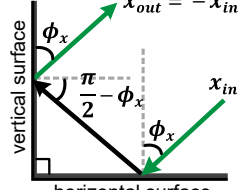


Fig. 8. Retro-reflection: outgoing signal has a reverse direction as incident one

### 3.1 Signal Enhancement by Increasing the Radar Cross Section of Vibration Point

The signal strength  $P_r$  received by the mmWave radar is expressed as [8]:

$$P_r = \frac{P_t G_t G_r \lambda^2 \sigma}{(4\pi)^3 R^4}, \quad (4)$$

where  $P_t$ ,  $G_t$ ,  $G_r$  refer to the radar transmitting power, Tx antenna gain, and Rx antenna gain, respectively.  $R$  is the distance between the point and radar.  $\sigma$  is called radar cross section (RCS). For the same radar and distance between radar and point, it is  $\sigma$  that determines the received signal strength  $P_r$ . RCS  $\sigma$  measures how easy the reflector can be detected by the radar, which is formulated as [1]:

$$\sigma = A_p \cdot p_r \cdot r_d, \quad (5)$$

where  $A_p$  is the project cross section which is decided by the point area.  $p_r$  refers to the reflectivity, which is determined by the point material.  $r_d$  denotes the directivity, which is defined as the ratio of the power reflected back in the radar's direction to the power radiating equally in all directions [14]. In other words, the directivity measures the concentration of reflector radiation pattern in the radar's direction. As the size and material of the vibration point are fixed,  $\sigma$  is mainly influenced by  $r_d$ . Thus, the more signal reflecting back to the radar's direction, the higher the  $r_d$  is. In practice, structures are mainly shaped in spheres, cylinders, and plates. However, as depicted in Fig. 7(a-c), these ordinary reflectors located in tilted directions to the radar would reflect away most of the incident signal to other directions (grey arrows) instead of back to the radar's direction, resulting in a low  $r_d$ . Then, the corresponding  $\sigma$  and  $P_r$  decrease. We conduct RCS simulation of spheres, cylinders, and plates using CST. The RCSs of the sphere, cylinder, and plate reflectors are as low as  $-40dBm^2$  to  $-30dBm^2$ . Thereby, we need to increase the directivity and RCS of the vibration point.

To achieve the above goal, we inspire from the retro-reflector, which can passively reflect the incident signal back to its reverse direction with increased  $r_d$  and  $\sigma$ , to design a point marker. There are primarily three types of retro-reflectors, including the Van Atta array, dihedral reflector, and trihedral reflector. We note that Van Atta arrays and dihedral reflectors can only achieve retro-reflection in a 2-dimension plane perpendicular to their surface [4, 5]. In real environments, due to the different locations and heights of multiple vibration points relative to the radar, the incident signal could come in different directions in the 3-dimension space. Therefore, we adopt the trihedral reflector which enables 3-dimension retro-reflection.

The principle of the trihedral reflector to increase the RCS stems from the construction of three conductive, intersected, and perpendicular surfaces, as depicted in Fig. 9. For simplicity, we explain the principle using two perpendicular surfaces at first. As shown in Fig. 8, the incident signal  $x_{in}$  has an AOA of  $\phi_x$  and gets reflected by the horizontal surface. Then, the signal arrives at the vertical surface, experiences the second reflection, and reflects back to the radar as  $x_{out}$ , whose angle of departure (AOD)  $\phi_x$  is the same as the AOA of  $x_{in}$ . As such, the ratio of signal reflecting back to the radar's direction over all directions, i.e., the signal directivity  $r_d$  and the RCS  $\sigma$ , is greatly improved. Then, adding a third perpendicular surface can further realize retro-reflection in 3 dimensions. We illustrate the RCS results for three typical forms of trihedral reflectors (i.e., cube, quarter circle, and triangle) in Fig. 11. Compared with the ordinary reflectors, the RCSs are significantly increased to

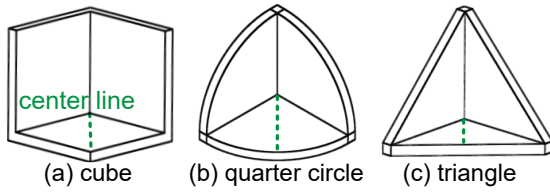


Fig. 9. Trihedral reflectors in cube, quarter circle, and triangle

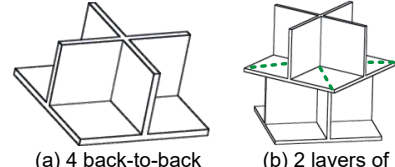


Fig. 10. Connected and layered trihedral reflectors

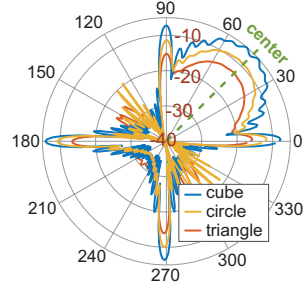


Fig. 11. RCS of three single trihedral reflectors

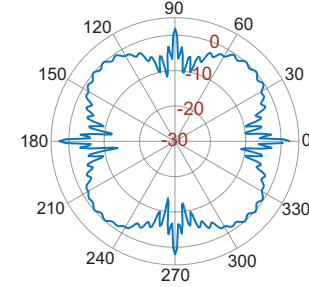


Fig. 12. RCS of four connected trihedral reflectors

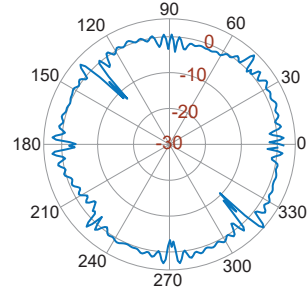


Fig. 13. RCS of two-layered trihedral reflectors

$-15dBm^2$  to  $-10dBm^2$  using trihedral reflectors. Besides, the trihedral cube reflector achieves the highest RCS, thus is selected to make the point marker.

We find that a single trihedral reflector achieves higher RCSs in  $\pm 30^\circ$  around its center line (i.e., boresight) but relatively lower RCSs near  $0^\circ - 15^\circ$  and  $75^\circ - 90^\circ$ . Such an imbalanced RCS improvement requires a strict or even fixed deployment of the marker and radar, making the system inconvenient and inflexible to use in practice. Thus, we further improve the design of the marker to ensure balanced RCS enhancement. Intuitively, we can widen the angle with an enhanced RCS by composing four trihedral reflectors, as depicted in Fig. 10(a), to cover the whole  $360^\circ$  angles. However, the four connected reflectors still fail to enhance the RCSs around conjunction areas. As shown in Fig. 12, the RCSs within  $\pm 10^\circ$  of  $0^\circ$ ,  $90^\circ$ ,  $180^\circ$ , and  $270^\circ$  are still not properly improved. To fully cover the entire  $360^\circ$  azimuth directions, we stack eight trihedral reflectors in two layers, with each layer consisting of four back-to-back reflectors. We dedicatedly align the center lines of the upper layer's reflectors with the vertical surfaces of the lower layer's reflectors, as shown in Fig. 10(b). As such, the four reflectors in the two layers can compensate each other, achieving the enhanced-RCS coverage over the whole  $360^\circ$  angles. The result of the layered reflector in Fig. 13 illustrates that the RCSs are evenly enhanced in almost all azimuth directions.

### 3.2 Implementation and Effectiveness of the Marker for Target Point Detection

Our point marker consists of a tiny 3D-printed skeleton of the trihedral reflector. Each side of the skeleton is a square plane (e.g.,  $2.5cm \times 2.5cm$ ). We print both single and layered trihedral reflectors as markers for different scenarios, as shown in Fig. 22(a). If the radar and makers' locations are fixed, we use the single one on the structure. Otherwise, we employ the layered one. The inner surface of each plane is coated by conductive materials with high reflection coefficients, e.g., copper and aluminum. Such a simply designed as well as a small-sized marker can be easily mounted on structures without affecting their vibrations. We tightly stick the markers to the target points on the structure using strong adhesive so that markers can vibrate synchronously with the target points.

We conducted experiments to verify the efficacy of our designed marker for point detection. We use three identical mini-motors as vibration points, which are separately placed, as shown in Fig. 14(a). First, we deploy the markers made from the single trihedral reflector on the left and right motors (markers 1 and 2), which are regarded as our target points. The motors are surrounded by static reflectors, such as desks and paper boxes.

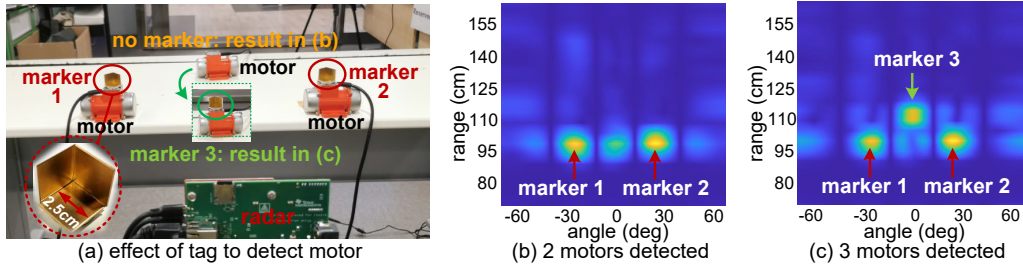


Fig. 14. Effect of the marker for vibration point detection: (a) deployment of the radar, mini-motors, and markers, (b) only 2 motors detected when using 2 markers, (c) all 3 motors are detected using 3 markers.

We configure the same parameters for all three motors and keep the surroundings unchanged throughout the experiment. The range-FFT and beamforming result in Fig. 14(b) shows that the left and right motors mounted with markers are clearly detected, while the middle motor without the marker and other nearby reflectors in the environment are not detected. Yet the middle motor can be successfully detected after being attached with marker 3, as depicted in Fig. 14(c). The experiment results manifest that our designed markers can significantly improve the detectability of target points and can be distinguished from other reflectors. We further apply our markers to the same blower machine in Fig. 6(a) for separately detecting the motor and wind box, as illustrated in Fig. 6(c). The result in Fig. 6(d) shows that two markers can be clearly detected, especially for the wind box, which fails to be detected without the marker.

#### 4 MULTI-VIB DESIGN FOR MULTI-POINT VIBRATION MONITORING

Fig. 15 illustrates the overview of Multi-Vib system for multi-point vibration monitoring. Multi-Vib consists of three key modules: (1) Point marker detection: detect the presence of target point markers and obtain their range bins and AOAs. (2) Signal separation: separate the signal reflected from each point marker. (3) Signal phase refinement: permute all antennas on the radar to generate different antenna arrays for removing the effect from static objects and obtain the accurate signal phase corresponding to the vibration signal. (4) Vibration measurement: estimate the vibration frequency and displacement of each point marker using the refined signal phase. In the following sections, we will introduce details of each module.

##### 4.1 Point Marker Detection

We first detect the point markers and locate their positions, including the range bin and AOA. To achieve this, we perform range-FFT and beamforming on the received intermediate frequency signal as introduced in Section 2.2 and Section 2.3, respectively. Since the marker has a higher RCS compared with nearby reflectors, it gives rise to higher signal power on the located range bin and AOA towards the radar. In Fig. 17(a), we depict the overall signal amplitude for each range bin. The amplitudes peak at the range bins where markers are located, i.e., the 10<sup>th</sup> and

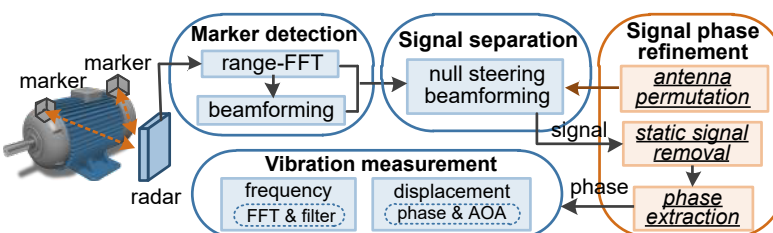


Fig. 15. Overview of Multi-Vib system for multi-point vibration monitoring

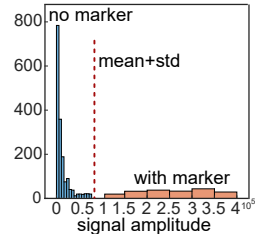


Fig. 16. Histogram of signal amplitude with and without markers

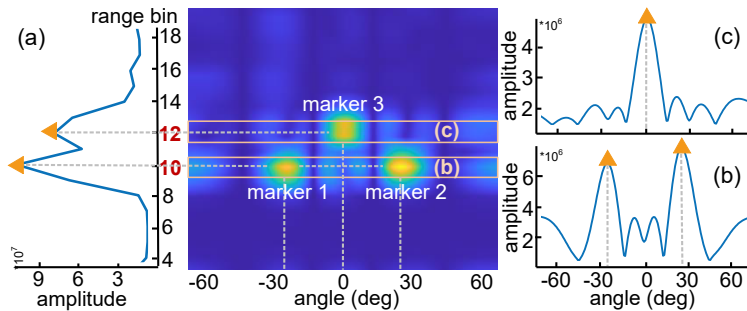


Fig. 17. Point marker detection from the signal amplitude: (a) detect the range bin of markers, (b-c) detect the AOA of markers

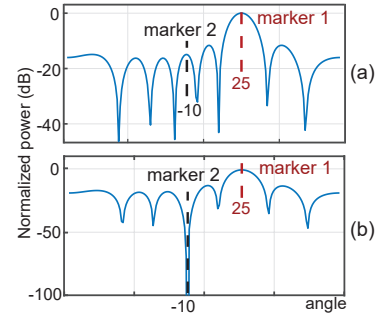


Fig. 18. Beamed pattern (a) before and (b) after beam nulling

12<sup>th</sup> range bin. Meanwhile, we show the signal amplitudes along different AOAs for the 10<sup>th</sup> and 12<sup>th</sup> range bin in Fig. 17(b) and Fig. 17(c), respectively. Similarly, the amplitude reaches an outstanding peak when the AOA equals the marker's direction to radar. Therefore, we search through range bins and AOAs to detect amplitude peaks. To avoid fake peaks, an empirical threshold is configured. We separately extract the amplitude of the signal along different range bins and angles with and without the point marker. Then, we illustrate their distributions as shown in Fig. 16. Next, we calculate the mean ( $\mu$ ) and standard deviation ( $\sigma$ ) of all signal amplitude and compare  $\mu$ ,  $\mu + \sigma$ ,  $\mu + 2\sigma$ ,  $\mu + 3\sigma$  with the former distributions. We find that the threshold of  $\mu + \sigma$  can effectively separate the two distributions as there is a clear gap between them. Thus, we set the threshold as  $\mu + \sigma$ . Peaks below this threshold can be simply discarded. Finally, we can obtain the range bin and AOA for each marker.

#### 4.2 Signal Separation

After point marker detection, we separate each marker's signal from  $Y(i, \phi, t)$  based on the detected range bin ( $i$ ) and AOA ( $\phi$ ) of each marker. However, if multiple markers are in the same range bin, signals reflected from different markers may interfere with each other due to the side lobes in the beamed pattern. As shown in Fig. 18(a), the beamed pattern towards marker 1 exhibits one main lobe and several side lobes. If marker 2 is located in the same range as marker 1 while in the direction of one side lobe generated by marker 1's beamed pattern, signals from marker 1 will be interfered by that of marker 2, resulting in an inaccurate vibration pattern from the signal phase. To show the side lobe effect, we place two mini-motors mounted with marker 1 and 2 in the same range bin and control them to vibrate separately at different frequencies. First, we use a high-end laser to measure marker 1's and marker 2's vibration displacement as ground truth, as shown in Fig. 19(c) and Fig. 19(a), respectively. Meanwhile, we extract marker 1's signal phase after range-FFT and beamforming and estimate its vibration displacement (will be introduced in Eq. (9)), as shown in Fig. 19(b). Compared with the ground truth of marker 1 with a single vibration frequency, the measured vibration pattern includes more than one frequency component, which is caused by the interference from marker 2's vibration. Hence, the side lobe effect should be removed to exclusively retrieve each marker's signal phase.

To achieve this, we leverage the null steering technique to annihilate the potential side lobes where interfering markers are located. Specifically, we aim to null the side lobe towards marker 2's direction to remove its interference on marker 1, as shown in Fig. 18(b). To this end, we need to obtain a new steering vector  $w_d$ , which can (1) preserve the main lobe towards the target marker's AOA ( $\phi_t$ ) and (2) null the side lobe towards the interfering marker's AOA. To meet requirement (1), the beamed pattern of  $w_d$ , especially for the main lobe, is expected to be as similar as that of the steering vector towards the target marker's AOA, i.e.,  $w(\phi_t)$ . Meanwhile, to satisfy requirement (2),  $w_d$  and the steering vector towards the interfering marker's AOA, i.e.,  $w(\phi_n)$ , should be orthogonal to each other [32]. Then, we can formulate an optimization problem to null the side lobe as follows:

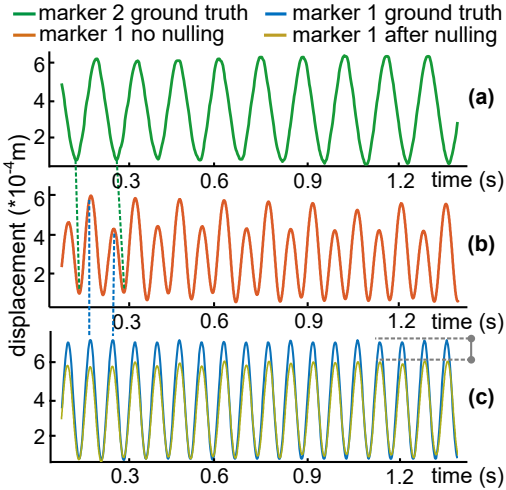


Fig. 19. (a) marker 2's vibration ground truth, (b) measured vibration of marker 1 before null steering, (c) marker 1's ground truth and measured vibration after null steering

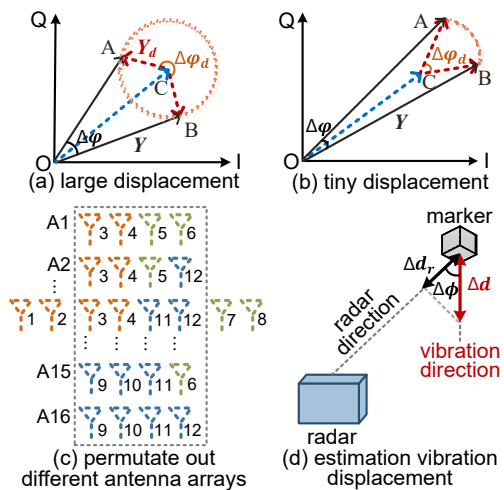


Fig. 20. Vibration measurement: (a-b) effect of static vector on signal phase, (c) antenna array permutation, (d) vibration displacement estimation

$$\begin{aligned} \min [w_d - w(\phi_t)]^H \cdot [w_d - w(\phi_t)], \\ \text{s.t., } w_d^H \cdot w(\phi_n) = 0, \end{aligned} \quad (6)$$

where  $(\cdot)^H$  is Hermitian transpose. The optimization problem can be solved by the Lagrange multiplier method. We leave the details to solve  $w_d$  in appendix A and show the result for one interfering marker (AOA:  $\phi_{n_1}$ ) as below:

$$w_d = w(\phi_t) - \frac{w(\phi_{n_1}) \cdot w(\phi_{n_1})^H}{w(\phi_{n_1})^H \cdot w(\phi_{n_1})} \cdot w(\phi_t) \quad (7)$$

Then, we apply the new steering vector  $w_d$  to perform beamforming and acquire the signal phase for each target point marker. In Fig. 19(c), we show marker 1's vibration pattern after nulling the side lobe in the yellow curve, whose vibration frequency exactly aligns with the real one measured by the laser.

#### 4.3 Signal Phase Refinement

In Fig. 19(c), we observe that extracted vibration displacement (yellow curve) exhibits a lower amplitude compared with the ground truth (blue curve). Such underestimated displacement is caused by the error-prone signal phase directly extracted from the signal after beamforming and null steering. Specifically, the separated signal inevitably involves the signal reflected from stationary objects around the points. As shown in Fig. 4(d), the received signal involves a static component that has zero velocity. Thus, the received signal vector  $\vec{Y}$  is actually a superposition of the static vector  $\vec{Y}_s$  of static objects and the dynamic vector  $\vec{Y}_d$  of the vibrating points as:  $\vec{Y} = \vec{Y}_s + \vec{Y}_d$ , as depicted in Fig. 20(a). The presence of  $\vec{Y}_s$  causes the actually measured phase  $\Delta\varphi$  to be smaller than the real phase  $\Delta\varphi_d$ . We need to remove the effect from the static vector to accurately measure  $\Delta\varphi_d$ .

We model the effect from static vector under different circumstances: (1) The vibration point has a relatively large displacement which is comparable to the half of the signal wavelength ( $\sim 3.89mm$ ). As such, the dynamic vector can rotate near a full circle, as shown in Fig. 20(a). However, the measured signal phase  $\Delta\varphi$  is smaller than the real one  $\Delta\varphi_d$  near  $2\pi$ . To retrieve  $\Delta\varphi_d$ , we can apply the circle fitting algorithm to estimate its center, which is the end point of static vector (i.e., point C), and subtract the center from the received complex signal to get rid of the static vector. The existing circle fitting algorithm is able to accurately estimate the center using a near full circle. Thus, the effect of static vector can be effectively removed. (2) The vibration point has a tiny

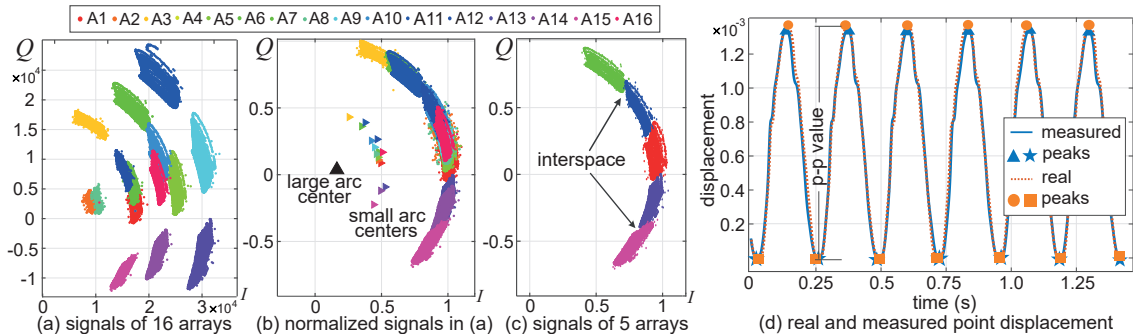


Fig. 21. Signal phase refinement: (a) beamformed signals of 16 antenna arrays, (b) scaled signals combined into a large arc, (c) scaled signals from 5 selected arrays, (d) marker vibration displacement using refined signal phase

displacement which is much smaller than the signal wavelength. In practice, the structure vibration is usually in a sub-millimeter level. In this way, the dynamic vector only forms a small arc, as depicted in Fig. 20(b). Since existing circle fitting is mainly an optimization problem, a smaller arc introduces more uncertainties in arc center estimation [2]. Thus, the estimated center with a small arc is error-prone, leading to unsuccessful removal of the static vector. (3) The arc becomes even smaller when the signal strength from static objects is stronger (i.e.,  $\|\vec{Y}_s\|$ ) while the vibration displacement is in sub-millimeter level (most cases in structure vibration). In a word, an effective method is demanded to accurately estimate the arc center for precisely removing the static vector and measuring the tiny vibration displacement. Previous works solve this issue by segmenting each chirp signal to generate multiple small arcs, which are translated and scaled to fit into a larger arc to estimate its center [18, 19]. However, segmenting the chirp inevitably sacrifices the range resolution, making it fail to differentiate closely located markers on a single structure.

To this end, we propose a new method, called antenna permutation, which effectively removes the static vector effect without sacrificing the range resolution. Specifically, we generate a larger arc by fully harnessing all antennas on the radar, i.e., virtual Rx 1-12 in Fig. 5(b). Conventionally, beamforming and null steering are performed on a single antenna array. While we jointly utilize the unused antennas RX 9-12 with Rx 3-6 to form multiple antennas arrays for separate null steering beamforming. The key insight of our method lies in two folds: (1) Rx 3-6 and Rx 9-12 are duplicated along the horizontal dimension. Thus, they can be mutually permuted into sixteen ( $\sum_{i=1}^4 C_4^i = 16$ ) sets of 4-element uniform linear antenna arrays and combined with Rx 1-2 and Rx7-8 for separate beamforming and null steering, as depicted in Fig. 20(c). Rx 9-12 introduces extra static phase offsets compared with Rx 3-6 as Rx 9-12 have an extra  $\lambda/2$  distance to Rx 3-6 in the vertical dimension. The extra static phase offset  $\varphi_p$  in the beamformed signal is determined by the number of antennas  $p \in \{0, 1, 2, 3, 4\}$  selected from Rx 9-12 and the elevation angle  $\theta$  between the radar and marker, which can be represented as below:

$$\varphi_p = p \cdot \pi \cdot \sin\theta \quad (8)$$

The  $\varphi_p$  will rotate the complex signals from different antenna arrays by various degrees in the IQ domain, resulting in multiple small arcs. Apart from the phase offset, the signal amplitude of different arrays also varies because of the antenna gain difference. In sum, due to amplitude variations and distinct phase offsets, the beamformed signals of different antenna arrays are distributed at different distances to the origin point as well as different angles to the I-axis. Note that all small arcs are intrinsically concentric as they are generated by the same vibration point. Therefore, we can merge these small arcs into a large arc. In Fig. 21(a), we show the complex signal of all sixteen permuted antenna arrays, which are indeed separately distributed in different quadrants with different amplitudes. Since the static and dynamic vectors are proportionally scaled based on the antenna gain, we normalize their amplitudes to the same scale and finally obtain a large arc in Fig. 21(b).

From Eq. (8), we have two main observations. First, as the  $p$  is fixed, the size of the generated large arc is affected by the  $\theta$ . A large  $\theta$  can increase  $\phi_p$  and potentially generate a larger arc. Intuitively, we can set a high elevation angle between the radar and marker to improve the center estimation accuracy. However, the elevation 3dB-beamwidth of the radar is within  $\pm 14^\circ$ . When  $\theta$  is out of the beamwidth, the radar signal strength significantly reduces. Fortunately, we find that a small  $\theta$  (e.g.,  $5^\circ$ ) can already make the signal vector rotate by almost quarter quadrant (i.e.,  $4 \cdot \pi \cdot \sin 5^\circ \approx 0.4\pi$ ) for a generating a large arc. Thereby, we place the radar slightly higher than the marker when monitoring the vibration. In addition, the effect of a small  $\theta$  on the displacement ( $\Delta d$ ) measurement is ignorable (e.g.,  $\Delta d \cdot \cos 5^\circ = \Delta d \cdot 0.996 \approx \Delta d$ ).

Second, five permuted antenna arrays, in which all  $p$  values are present, can form a large arc with a similar size to the arc generated from all sixteen antenna arrays, as shown in Fig. 21(b) and Fig. 21(c). In other words, we may obtain an acceptable center estimation from the selected five antenna arrays. While we find that the large arc becomes more complete if more antenna arrays are involved. As shown in Fig. 21(c), there are interspaces along the large arc formed by the five selected arrays as the edges of small arcs do not strictly overlap. However, these interspaces can be filled up by the arcs formed by remaining arrays, as depicted in Fig. 21(b). Most importantly, the combined arc from all sixteen antenna arrays is slightly larger than that from the five selected arrays. This is because different antennas bare inherent and random phase offsets incurred by the hardware imperfections which turn out to be a benefit for us because they contribute to forming a larger and thorough arc, improving the accuracy for arc center estimation. Therefore, in our work, we utilize all the sixteen antenna arrays to estimate the arc center and remove the static vector. We first apply the time-efficient Taubin fit method [30] to estimate an initial arc center and radius. Then, the initial results are input as the first guess to the geometric Levenberg-Marquardt fit method [12], which can further improve the circle fitting accuracy. As depicted in Fig. 21(b), compared with the arc centers estimated by small arcs, the large arc can provide a broader view of the original circle, making the estimated circle center more accurate. Note that applying all sixteen antenna arrays does not pose much extra overhead as the null steering can be efficiently performed via vector multiplication.

Finally, we subtract the estimated center from the normalized and complex signal samples and obtain the refined signal phase for each antenna array. Since different antenna arrays' signals are affected by the same vibration point, we select the refined signal phase from one antenna array whose signal has the highest amplitude because a relatively larger antenna gain and signal amplitude can tolerate more inherent phase noises.

#### 4.4 Vibration Displacement and Frequency Estimation

Based on the refined signal phase change  $\Delta\varphi(t)$  and the geometric relationship between the marker and radar, as shown in Fig. 20(d), we can derive the vibration displacement change  $\Delta d(t)$  along the vibration direction as follows:

$$\Delta d(t) = \frac{\Delta d_r(t)}{\cos\phi} = \frac{\Delta\varphi(t) \cdot \lambda}{4\pi \cdot \cos\phi_m}, \quad (9)$$

where  $\Delta d_r(t)$  is the displacement towards the radar direction, and  $\phi_m$  is the marker AOA.

With the obtained vibration displacement pattern, we first perform FFT on the displacement signal after removing the DC component for vibration frequency analysis. If the marker vibrates with a single frequency, only one peak outstands the noise level in the frequency-domain spectrum. The spectrum noise level is empirically set as the mean of all spectrum amplitudes. The frequency corresponding to the peak is the estimated vibration frequency  $f_s$ . Then, we calculate the vibration displacement by measuring the peak-to-peak (p-p) value [16, 26]. To obtain the p-p value, we apply the peak detection algorithm, which detects the local maximum and minimum, on the displacement signal to extract the upper and lower peaks, as highlighted by the triangle and star markers in Fig. 21(d). Then, the p-p value is the distance between adjacent upper and lower peaks. To avoid mis-regarding the smaller fluctuations in the displacement signal as peaks, we apply a bandpass filter to smooth the signal. The lower and higher cutoff frequencies of the bandpass filter are set as  $f_s - 1\text{Hz}$  and  $f_s + 1\text{Hz}$ , respectively.

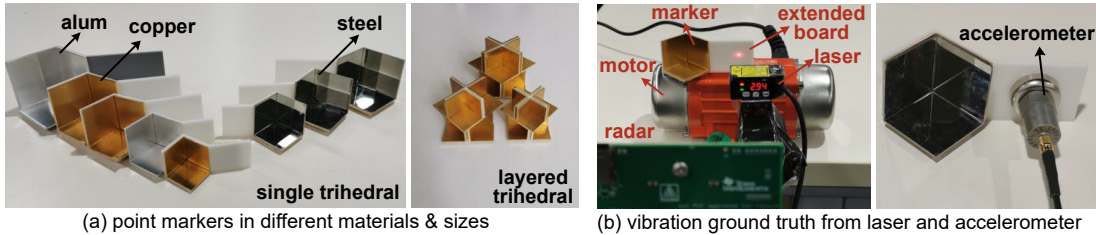


Fig. 22. Illustration of point markers and setup for measuring the vibration ground truth: (a) Point markers in different sizes, materials, and forms, (b) laser and accelerometer to measure vibration ground truth on machine, shake table, and bridge

In practice, structures could vibrate with several frequencies when bearing problems, leading to multiple frequency peaks in the spectrum. Under multi-frequency circumstances, we first estimate all vibrating frequencies after FFT. For each frequency  $f_i$  above the noise level, we also employ the bandpass filter to remove the effect of other frequencies. Then, we apply peak detection to extract the p-p value of vibration displacement for each  $f_i$ . In Section 5.5, we will show how vibration frequency and displacement help to detect structural impairments.

## 5 EVALUATION

In this section, we introduce the experiment setup and evaluation results of Multi-Vib.

### 5.1 Experiment Setup and Evaluation Methods

**5.1.1 Implementation.** The Multi-Vib system is implemented with a commercial mmWave radar, Texas Instruments (TI) AWR1843BOOST, which works on the 77 – 81GHz frequency band and equips with 3 Tx and 4 Rx antennas. Tx antennas send FMCW chirp signals with 3.6GHz bandwidth. The signal is collected using TI DCA1000EVM in real time. The sampling rate of radar signal is set to 2KHz, which can sense the vibration with up to 1MHz frequency. The signal is processed in Matlab on a computer with an Intel i7-9750H processor and 16GB memory. In the beamforming step to obtain each marker's AOA, we sweep the angle between  $[-90^\circ, 90^\circ]$  with a resolution of  $1^\circ$  using a short period of signal (1s), which costs around 1.5s in total. Note that the angle sweeping in only needs to be performed once to detect vibration points, which is a one-time step at the beginning of vibration monitoring. The computation cost of the null steering optimization problem is  $O(n)$ , where  $n$  is the length of the steering vector. The skeleton of the point marker is 3D-printed using the Poly Lactic Acid (PLA) filament. Then, different metal materials, including brass copper, aluminum, and 304 stainless steel, are coated on the inner side of the marker skeleton, as shown in Fig. 22(a). We also make markers in different sizes to investigate the effect of marker size on the detection range and angle. The average cost of the marker is around USD 5.

**5.1.2 Experiment Scenarios.** We conduct experiments in a mechanical lab, industrial center, and bridge. We use mini-motors to act as vibration points, as shown in Fig. 14(a) and Fig. 22(b), and evaluate the performance of point detection, vibration frequency, and displacement estimation with respect to different numbers of points, different vibration frequencies and displacements, different distances and angles between radar and points. The vibration frequency and displacement of mini-motors are controlled via a speed and voltage controller. We also apply Multi-Vib to monitor the vibration of real-world structures with the following case studies: (1) conveyor machine, which is widely used in production plants to deliver materials and goods. (2) structural dynamics analysis, which refers to the analysis of a structure's responses to dynamic loads. This analysis is widely used in civil engineering research studies. (3) bridge vibration, which serves as an essential indicator of the bridge health condition.

**5.1.3 Ground Truth.** The vibration ground truth is mainly obtained using a laser vibrometer, Panasonic HL-G105-S-J, which has a detection range of  $\pm 4\text{mm}$  and a high precision of  $0.5\mu\text{m}$ . In Fig. 22(b), the laser is placed on a stationary tripod in front of the marker. We print a extended plane board besides the marker as a reflector of the laser beam. In this way, the vibration displacement measured from the laser is the same as that of the marker. For

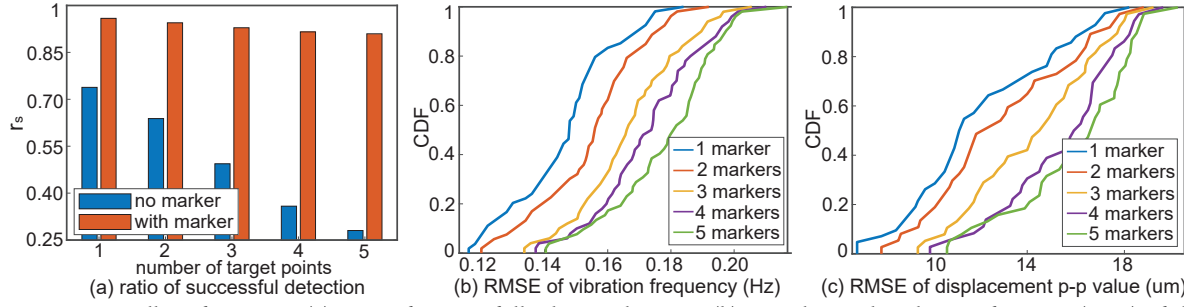


Fig. 23. Overall performance: (a) ratio of successfully detected points, (b) cumulative distribution function (CDF) of the RMSE in vibration frequency estimation, (c) CDF of the RMSE in vibration displacement p-p value estimation

the bridge vibration, its ground truth is obtained using a single-axis accelerometer (ICP/IEPE CT1005LC) with a sensitivity of  $50mV/g$ , as depicted in Fig. 22(c). The reason why we do not use the laser to measure the ground truth of bridge vibration is that the laser needs to be mounted on a stationary support close to the vibration point. However, since the bridge keeps vibrating, we can hardly find a place to deploy the laser on the bridge.

**5.1.4 Evaluation Metrics.** First, we define the ratio of successful point detection as the number of successful detection of each marker over all trials to evaluate the effectiveness of our designed markers. Second, we employ the root mean square error (RMSE) between the real and estimated vibration frequencies and displacement p-p values to evaluate the vibration measurement accuracy. In Multi-Vib, we divide the received signal into short and fixed-length windows (e.g., 2s) for real-time vibration monitoring. For each window, the real and estimated vibration frequencies and average displacement p-p values are obtained from the laser and radar signal, respectively. The RMSE of vibration frequency is given by  $\sqrt{\frac{1}{N} \sum_{i=1}^N (f_i^2 - \hat{f}_i^2)}$ , where  $f_i$  and  $\hat{f}_i$  refer to the real and estimated vibration frequencies in window  $i$ , respectively, and  $N$  is the total number of windows. Likewise, the RMSE of vibration displacement p-p value can be obtained from the real and estimated p-p values  $d_i$  and  $\hat{d}_i$ .

## 5.2 Overall Performance

**5.2.1 Vibration Point Detection.** The average ratio of successful vibration point detection is 0.948. First, we show the performance of vibration point detection using our designed markers. We select one to five mini-motors as vibration points and randomly change their distances to the radar within  $2 - 4m$  and their angles to the radar within  $\pm 40^\circ$ . We first detect mini-motors without attaching the marker for comparison. Then, 3cm-size markers (the single one) are attached to each mini-motor. The result of successful point detection ratio is given in Fig. 23(a). Our designed markers can significantly improve the ratio ( $r_s$ ) by around 45% on average. Moreover,  $r_s$  drops dramatically with the increasing number of points without the marker. This is because points that are farther or have a tilted angle to the radar can be missed. When equipped with markers,  $r_s$  only experiences a slight decrease even for five points. This indicates that the marker can effectively increase the detectability of multiple points.

In addition, we deliberately put some static objects, e.g., boxes and shelves, around the mini-motors attached with markers during experiments. Notably, our designed markers present a higher detectability than these objects due to the retro-reflective property of trihedral reflectors. The false positive ratio of regarding surrounding objects as the vibration points is 6.3%. The mere wrong detection mainly comes from the presence of large doors and guards. Nevertheless, these false negatives can be removed by analyzing their reflected signal phase, which is relatively stable without a changing vibration pattern.

**5.2.2 Vibration Frequency and Displacement p-p Value.** The median RMSEs of estimating vibration frequency and displacement p-p value are around 0.16Hz and 14.5um, respectively. We present the overall performance of

Table 1. Comparison of Multi-Vib with state-of-the-art systems.

	error of frequency	error of displacement	multi-point measurement
TagSMM [35]	0.3-0.8Hz	10-40um	Not applicable
mmVib [19]	0.1-0.3Hz	5-15um	Not applicable
<b>Multi-Vib</b>	<b>0.1-0.2Hz</b>	<b>7-18um</b>	<b>Yes</b>

estimating the vibration frequency and displacement p-p value for different numbers of vibration points ( $n_t$ ) attached with the single trihedral marker, which are driven by mini-motors with different vibration frequencies (10 – 50Hz) and displacements (0.05 – 2mm). For  $n_t = 2$  and  $n_t = 3$ , two markers and three markers with a separation of 15° – 60° between each other are placed in the same range bin, respectively. For  $n_t = 4$ , we divide the four markers into two groups, and each group's two markers are located in the same range bin. For  $n_t = 5$ , two of the markers are in the same range bin, and the left three markers are in different bins. The distance between markers in different range bins is set within the range of 15 – 50cm.

As depicted in Fig. 23(b), Multi-Vib can achieve a median RMSE of 0.144Hz for estimating the vibration frequency for one point. The median RMSE increases by only 0.05Hz when the number of points grows to five. Meanwhile, the median RMSE for estimating the displacement p-p value, as shown in Fig. 23(c), is within 10.5 – 16.1um across different numbers of points. In addition, we compare the RMSE of displacement p-p value with and without our antenna permutation method for signal phase refinement. The antenna permutation method can decline the RMSE by around 28% of the displacement p-p value estimated from the raw signal phase after range-FFT and beamforming, showing the efficacy of our phase refinement method.

**5.2.3 Comparison with State-of-the-art Works.** We compare the performance of Multi-Vib with two state-of-the-art systems, i.e., TagSMM [35] and mmVib [19]. TagSMM employed the RFID signal reflected by the vibrating object from multiple nearby RFID tags for vibration measurement. mmVib utilized the mmWave radar for vibration monitoring. The comparison details are shown in Table 1. Compared with TagSMM, Multi-Vib can measure the vibration frequency and displacement with higher accuracy. Besides, TagSMM only considers measuring a single object's vibration. Compared with mmVib, Multi-Vib achieves a similar error in frequency estimation but a slightly higher error in displacement estimation. This is because Multi-Vib faces stronger interference from multiple points. Although mmVib can measure multiple objects' vibrations, it is not applicable for multi-point measurement due to the following reasons. First, the whole object (e.g., the whole machine) can reflect a larger portion of signal back to the radar than the small point. Thus, multiple objects can be more easily detected by the radar. Second, mmVib sacrifices the range resolution for accurate vibration measurement. However, compared with the far distance between multiple objects, the close points on a single object require a higher range resolution. By contrast, Multi-Vib can effectively detect multiple points and maintain the range resolution.

### 5.3 Effect of Vibration Frequency and Displacement Level

We evaluate the accuracy of Multi-Vib on estimating vibration frequency and displacement p-p value considering the effect of different levels of vibration frequencies and displacements of vibration points. In following experiments, we use two 3cm-size single trihedral markers with 2 – 3m distance and 0° – 30° angle to the radar.

**5.3.1 Different Frequency Levels.** The RMSEs of frequency and displacement p-p value estimation for lower frequency levels (< 20Hz) are 0.015Hz and 2.6um larger than those of higher levels (> 20Hz). We adjust the vibration frequency of mini-motors using the speed controller with different levels, including 5 – 10Hz, 10 – 20Hz, 20 – 30Hz, 30 – 40Hz, 40 – 50Hz, and 50 – 100Hz. The vibration displacement is kept in the range of 0.5 – 1mm. The RMSEs of frequency estimation and displacement p-p value estimation among different frequency levels are shown in Fig. 24(a) and Fig. 24(b), respectively. Lower frequency levels (i.e., 5 – 10Hz and 10 – 20Hz) lead to relatively larger errors in both frequency (mean RMSE of 0.126Hz) and displacement p-p value (mean RMSE of 15.6um) estimation compared

with those of higher frequency levels (mean RMSE of  $0.112\text{Hz}$  and  $13.2\mu\text{m}$ ). The main reason is that vibrations with lower frequency levels are more vulnerable to irregular noises and fluctuations in the vibration pattern.

**5.3.2 Different Displacement Levels.** The RMSEs of frequency and displacement p-p value estimation for smaller displacement levels ( $< 0.3\text{mm}$ ) are  $0.035\text{Hz}$  and  $7.2\mu\text{m}$  larger than those of higher levels ( $> 0.3\text{mm}$ ). We adjust the vibration displacement of mini-motors using the voltage controller with different levels, including  $0.05 - 0.1\text{mm}$ ,  $0.1 - 0.3\text{mm}$ ,  $0.3 - 0.5\text{mm}$ ,  $0.5 - 1\text{mm}$ ,  $1 - 2\text{mm}$ , and  $2 - 3\text{mm}$ . The vibration frequency level is kept within  $30 - 40\text{Hz}$ . The RMSEs of frequency estimation and displacement p-p value estimation among different displacement levels are shown in Fig. 25(a) and Fig. 25(b), respectively. Smaller displacement levels, especially within  $0.05 - 0.1\text{mm}$ , result in larger RMSEs for both frequency (mean RMSE of  $0.162\text{Hz}$ ) and displacement p-p value (mean RMSE of  $18.1\mu\text{m}$ ) estimation due to the reason that tiny displacement can be more easily overwhelmed by noises. When the displacement level is above  $0.5\text{mm}$ , RMSEs drop to  $10 - 12\mu\text{m}$ .

#### 5.4 Effect of Distance, Angle, and Marker Size

The distance and angle between the radar and marker may affect the performance of marker detection and vibration measurement. Besides, the marker size also influences the effective detection range, including distance and angle. Thereby, we conduct experiments to investigate the joint impact from distance, angle, and marker size on the vibration monitoring performance. In the following experiments, the vibration frequency and displacement of the mini-motor attached with one marker are kept at  $20 - 30\text{Hz}$  and  $0.5 - 1\text{mm}$ , respectively.

**5.4.1 Marker Size Effect on Detection Distance.** The marker with side lengths of  $3\text{cm}$  and  $6\text{cm}$  can be detected within  $4\text{m}$  and  $8\text{m}$  to the radar, respectively. We attach the single trihedral marker with different sizes ( $2\text{cm}$ ,  $2.5\text{cm}$ ,  $3\text{cm}$ ,  $3.5\text{cm}$ ,  $4.5\text{cm}$ , and  $6\text{cm}$ ) on the mini-motor and set different distances  $d_0$  between the marker and radar ( $0.8\text{m} - 1\text{m}$ ,  $1\text{m} - 2\text{m}$ ,  $2\text{m} - 3\text{m}$ ,  $3\text{m} - 4\text{m}$ ,  $4\text{m} - 5\text{m}$ ,  $5\text{m} - 6\text{m}$ , and  $6\text{m} - 8\text{m}$ ). The marker is placed perpendicular to the radar. The results of frequency and displacement p-p value estimation are given in Table 2. For the marker with  $2 - 2.5\text{cm}$  side length, the radar can successfully measure its vibration within  $3\text{m}$  with an average error of  $0.16\text{Hz}$  in frequency estimation and  $16.4\mu\text{m}$  in displacement estimation. For distances above  $3\text{m}$ , a larger side length of the marker (e.g.,  $3\text{cm}$ ) is demanded. According to our experiment results, the marker with size of  $6\text{cm}$  can be detected as far as  $8\text{m}$  to the radar with average errors of  $0.137\text{Hz}$  and  $15.8\mu\text{m}$  in vibration frequency and displacement estimation, respectively, which is enough for indoor machine monitoring. For monitoring large civil structures, the compact markers can be flexibly placed for local vibration measurement at some risky points. We also evaluate the performance of the layered trihedral marker, which achieves a similar result as the single one. This is because the layered marker is designed to evenly enhance the RCS over all  $360^\circ$  azimuth directions while the maximum RCS remains the same as the single trihedral marker when being placed perpendicular to the radar. Another observation is that for the same  $d_0$ , the larger marker can improve the estimation accuracy. While,

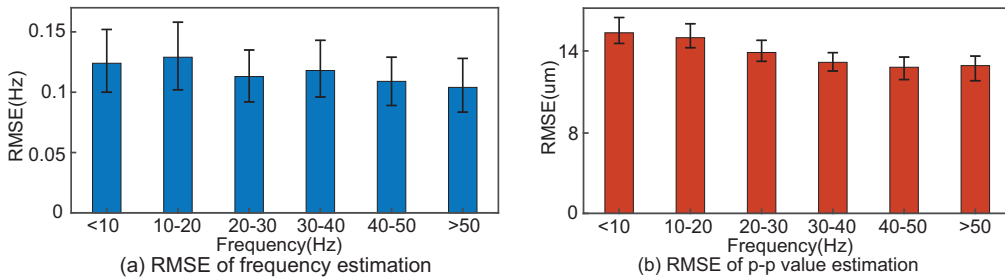


Fig. 24. Effect of vibration frequency levels on the accuracy of estimating frequency and displacement p-p value

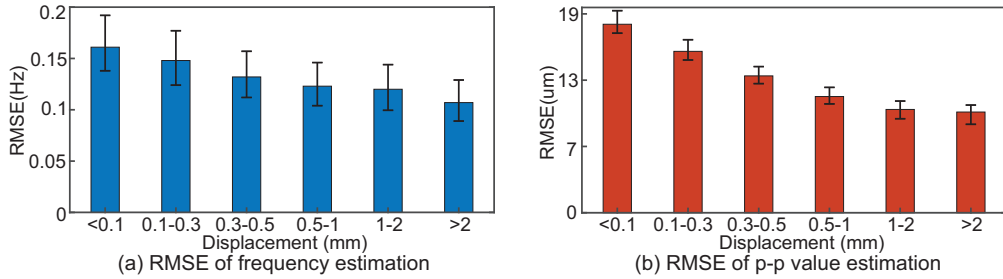


Fig. 25. Effect of vibration displacement levels on the accuracy of estimating frequency and displacement p-p value

the RMSE increases with longer  $d_0$  for the same size of marker. This is because the signal-to-noise ratio (SNR) is decreased for longer distances.

**5.4.2 Marker Size Effect on Detection Angle.** The single trihedral marker with side lengths of 2.5cm and 6cm can be detected within 30° and 45° angle to the radar, respectively. The layered trihedral marker can cover up to 50° with a side length of 2cm and above. We first evaluate the performance of the single trihedral marker by changing the angle between the radar and the marker, i.e., 0° – 10°, 10° – 20°, 20° – 30°, 30° – 40°, 40° – 45°, and 45° – 90°. The distance between the marker and radar is set to 2m. We show results of frequency and displacement p-p value estimation for different angles in Table 3. When the marker is placed within 40° to the radar, a side length of 3cm enables the marker to be effectively detected. Markers whose side lengths are above 4.5cm are detected within 45° to the radar. Meanwhile, we also evaluate the layered trihedral marker, which can already cover up to 50° angle with a side length of 2cm as the two layers of trihedral reflectors can jointly improve the RCS with a wider angle range. However, when the angle is above 50°, we fail to detect the marker because the radar's 6dB beamwidth is around ±50° [6], making the radar signal strength significantly declines out of ±50°. Nevertheless, as the beamwidth is symmetric at 0°, we can still achieve up to around 100° width of detection angles.

Table 2. RMSEs of frequency (freq, Hz) and displacement p-p value (p-p, um) estimation for different distances between the radar and vibration points with respect to different marker sizes (single trihedral reflector).

$d_0$	0.8m-1m		1m-2m		2m-3m		3m-4m		4m-5m		5m-6m		6m – 8m	
	freq	p-p	freq	p-p	freq	p-p	freq	p-p	freq	p-p	freq	p-p	freq	p-p
2cm	0.142	13.8	0.152	15.6	0.160	16.4	/	/	/	/	/	/	/	/
2.5cm	0.138	13.5	0.149	15.3	0.151	15.8	/	/	/	/	/	/	/	/
3cm	0.134	13.1	0.137	13.9	0.142	14.5	0.141	15.1	/	/	/	/	/	/
3.5cm	0.131	12.8	0.129	13.4	0.136	13.8	0.137	14.2	0.134	14.9	/	/	/	/
4.5cm	0.128	12.4	0.126	13.0	0.129	13.3	0.131	13.7	0.128	13.9	0.132	14.8	/	/
6cm	0.121	11.5	0.123	12.1	0.125	12.7	0.126	13.2	0.126	13.6	0.129	14.5	0.137	15.8

Table 3. RMSEs of frequency (freq, Hz) and displacement p-p value (p-p, um) estimation for different angles between the radar and vibration points with respect to different marker sizes (single trihedral reflector).

angle	0° – 10°		10° – 20°		20° – 30°		30° – 40°		40° – 45°		45° – 90°	
	freq	p-p	freq	p-p	freq	p-p	freq	p-p	freq	p-p	freq	p-p
2cm	0.158	16.5	0.154	17.0	0.161	17.5	/	/	/	/	/	/
2.5cm	0.152	16.1	0.152	16.7	0.159	17.2	/	/	/	/	/	/
3cm	0.144	15.6	0.149	16.3	0.155	16.9	0.162	17.4	/	/	/	/
3.5cm	0.12	15.2	0.143	15.6	0.148	15.9	0.151	16.6	/	/	/	/
4.5cm	0.130	14.5	0.133	14.7	0.135	14.9	0.141	16.3	0.161	18.9	/	/
6cm	0.129	13.4	0.130	14.1	0.132	14.4	0.136	15.7	0.154	17.6	/	/

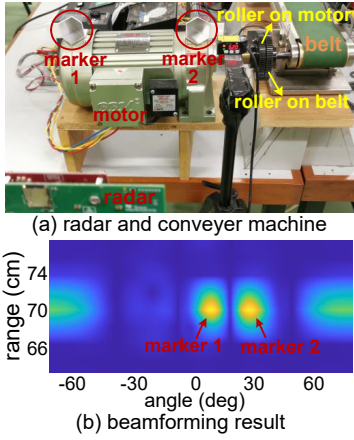


Fig. 26. Conveyor machine monitoring: (a) deployment of radar, marker, and machine, (b) beamforming result

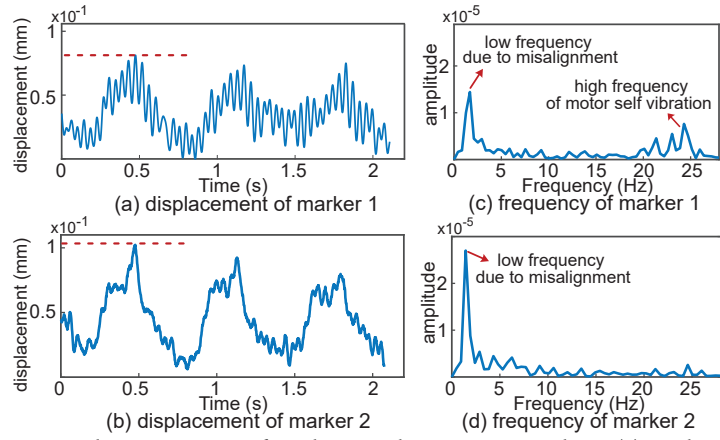


Fig. 27. Vibration pattern of markers on the conveyor machine: (a) marker 1's displacement pattern, (b) marker 2's displacement pattern, (c) marker 1's FFT result, (d) marker 2's FFT result

## 5.5 Case Studies

In this section, we apply the Multi-Vib system to monitor machines and civil structures to evaluate its performance in several important real-world applications.

**5.5.1 Conveyor Machine Vibration Monitoring.** The widely used conveyor machines in plants are vulnerable to the misalignment problem, which is caused by the mismatch between the roller from the motor and the roller connected with the belt, as shown in Fig. 26(a). The misalignment issue will cause the motor to vibration with the rolling frequency. In this case study, we attach two markers (marker 1 and marker 2) to the left and right points on the conveyor machine, which already suffers from the misalignment problem, and monitor the machine vibration. We first apply range-FFT and beamforming to detect the two markers, as depicted in Fig. 26(b). Then, we extract each marker's signal phase and displacement, as shown in Fig. 27(a-b). Finally, we perform FFT on the displacement and obtain the spectrum in Fig. 27(c-d).

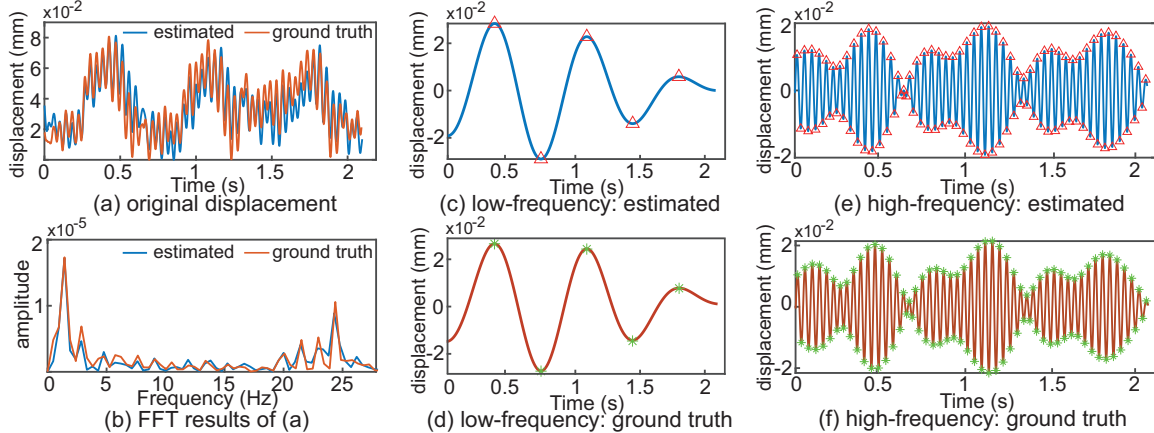


Fig. 28. (a) original displacement change from the radar signal and the laser, (b) FFT results of displacement change, (c) low-frequency displacement estimated by radar signal, (d) low-frequency displacement measured by laser, (e) high-frequency displacement estimated by radar signal, (f) high-frequency displacement measured by laser

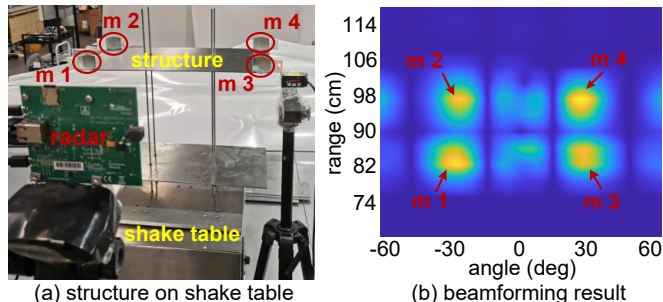


Fig. 29. Structure dynamics analysis on shake table: (a) shake table, structure, markers (m1-m4), and radar, (b) beamforming result

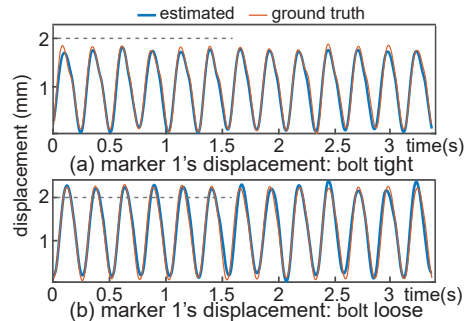


Fig. 30. Vibration pattern of marker 1: (a) with tight bolt, (b) with loose bolt

From the two points' spectrum, we can observe an outstanding low-frequency component, which exactly corresponds to the rolling frequency. Meanwhile, marker 2 exhibits a larger displacement and a higher amplitude on the low-frequency component in the spectrum than those of marker 1. This is mainly because marker 2 suffers more from the misalignment issue as it is closer to the roller. These observations indicate the presence of the roller misalignment problem as well as telling which part of the machine is more problematic. The high-frequency components in marker 1's spectrum are caused by the inherent vibration of the working motor, which only accounts for a small proportion of the whole spectrum. The insignificant high-frequency component infers that the motor itself still runs healthily.

Next, we evaluate the accuracy of estimating the frequency and displacement p-p value for the conveyor machine. As shown in Fig. 28(a), we use a laser to measure marker 1's vibration ground truth. Then, we perform FFT on marker 1's real and estimated displacements from the laser and radar signals, respectively, as depicted in Fig. 28(b). The peak frequencies, including both low-frequency and high-frequency components, of the real and estimated vibration closely match each other. Then, we apply bandpass filters to obtain the low-frequency and high-frequency displacement patterns, as shown in Fig. 28(c-f). Compared with the ground truth, the displacement peaks are accurately detected from the measured radar signal. The average RMSE in frequency estimation for the two markers is 0.13Hz, and the average RMSE of displacement p-p value estimation is 14.8um.

**5.5.2 Structure Dynamics Analysis.** Monitoring and analyzing the structure's responses under dynamic loads (e.g., earthquake and wind) is crucial for designing structures to withstand severe disasters and weather conditions. In civil engineering, researchers simulate various dynamic loads to structures and measure their dynamic responses, including displacement, velocity, and acceleration. The shake table is one of the common tools to generate and simulate dynamic loads [9, 34]. Traditionally, displacement sensors (e.g., laser and linear variable differential transformer) and accelerometers are employed to measure the structure response on the shake table, which can be quite costly and inconvenient. In this case study, we substitute conventional sensors with our vibration markers to investigate the effectiveness of Multi-Vib for measuring the structure's dynamic responses.

As shown in Fig. 29(a), we build a two-story steel structure and mount it on a shake table. We attach markers to the four points at each corner of the structure and separately monitor their vibrations. The four markers are successfully detected after range-FFT and beamforming, as depicted in Fig. 29(b). The structure is excited with a 4Hz sine wave as the input motion generated by the shake table. Then, we tighten all the bolts on the structure and extract all markers' vibration patterns. For example, the estimated and ground-truth displacements of marker 1 from the radar signal and laser are illustrated in Fig. 30(a). Next, we loosen the bolt between the steel plate and the rod on the lower-left corner around marker 1, which incurs a structure damage called bolt loose. The bolt loose results in a decrease in the structure's stiffness, which increases its displacement under the same input motion, especially for the area around the lower-left bolt (e.g., marker 1's position). As depicted in Fig. 30(b),

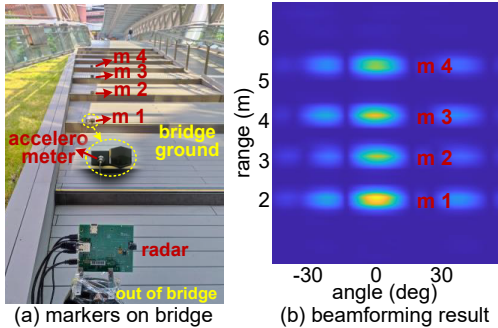


Fig. 31. Bridge vibration monitoring: (a) bridge, markers, and radar (b) beamforming result

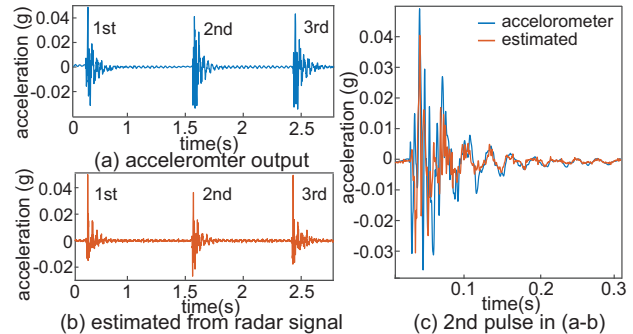


Fig. 32. Bridge vibration: (a) acceleration output of three hits from accelerometer and radar signal (b) detailed acceleration of 2nd hit

the extracted displacement of marker 1 under the bolt loose is indeed about 0.3mm larger than that with the tight bolt. Meanwhile, marker 1 experiences more displacement growth than the other three markers (especially markers 3 and 4) because the bolt loose happens around marker 1. Therefore, we can detect the location of bolt loose from the displacement change of four markers. In this case study, the average RMSEs for estimating the structure's vibration frequency and displacement p-p value are 0.11Hz and 12.5um, respectively.

**5.5.3 Bridge Vibration Monitoring.** Vibration is an essential indicator for evaluating bridge health conditions. Existing approaches mainly install accelerometers to monitor bridge vibration caused by external forces, e.g., passing vehicles and wind. However, for short-span bridges (length within 20–30m), accelerometer-based systems may not be an efficient solution for a large number of short bridges in many cities because of the sensor and installation cost. Therefore, we attempt to apply the Multi-Vib system for monitoring short bridges' vibration.

As shown in Fig. 31(a), we mount four vibration markers (m1-m4) on each step of the footbridge. In this way, we can acquire the vibration responses at multiple steps for more fine-grained bridge vibration monitoring. The mmWave radar is placed on the stable ground outside the bridge. As illustrated in Fig. 31(b), all the four markers are successfully detected after range-FFT and beamforming. Then, we find volunteers and ask them to walk and hit the ground of each step. These hits can incur pulse vibrations on the bridge ground. To compare our extracted vibration pattern from the radar signal with the ground truth, we employ a high-precision accelerometer and attach it to the extended board out of the marker to measure the acceleration ground truth.

We calculate the acceleration by taking the second derivative of displacement extracted from the radar signal and compare it with the acceleration ground truth. Taking the step mounted with marked 1 as an example, its real and estimated acceleration are depicted in Fig. 32(a) and Fig. 32(b), respectively. Multi-Vib can effectively detect each hit on the step. We also compare the detailed acceleration signal. As shown in Fig. 32(c), even though the estimated acceleration misses a few tiny fluctuations, the general patterns of the acceleration estimated from the radar signal and that from the accelerometer can match each other. The mean correlation between the estimated and real acceleration of all hits on different steps is around 0.65. Meanwhile, we extract the distance between the highest and lowest peak from each hit's acceleration signal and calculate the difference between our estimated values and the actual values acquired from the accelerometer. The average difference is 10.5% over the actual value. This indicates that our system can retrieve a similar vibration acceleration pattern as the accelerometer.

## 6 RELATED WORK

In this section, we introduce and compare existing systems that are related to vibration monitoring.

### 6.1 Accelerometer-based Vibration Monitoring

There are mainly three types of accelerometer, including piezoelectric, piezoresistance, and capacitive accelerometer. The piezoelectric accelerometers are mostly used for vibration measurement because it is more sensitive to tiny acceleration changes [24, 28]. Although accelerometers can provide precise measurement of vibrations, it fails to output accurate displacement because the integration operation can accumulate and exaggerate measurement errors in the displacement. There are many systems that provide multiple accelerometer channels for multi-point acceleration measurement at the same time. However, these systems are quite expensive due to the increasing number of sensors and channels for data collection. In addition, accelerometers need extra power supplies, which add more installation complexity in real environments.

### 6.2 Light-based Vibration Monitoring

Laser vibrometers and cameras enable a non-contact way for monitoring the vibration. Lasers can directly measure the vibration displacement by calculating the change of the laser light's traveling distance reflected by the vibrating object [20, 21]. Lasers can enable fine-grained measurement of displacement with  $\mu\text{m}$  resolution. However, it also shows some drawbacks in real-world usage. First, lasers are mainly used to measure vibrations in short ranges (usually within 2m) because the laser light can be easily occluded by surrounding objects. Therefore, lasers are not proper for remote monitoring of vibrating objects. Second, a high-precision laser is rather costly. This could raise the expense for employing multiple lasers to realize multi-point vibration simultaneously.

High-definition cameras are usually employed to extract pixels which become individual point sensors for vibration measurement [10, 11]. The change of pixel contour can infer the vibration pattern along the time. However, high-resolution cameras are relatively expensive. Thus, recent studies have been trying to ease the high cost and high definition requirement for cameras and propose motion magnification techniques to extract the vibration pattern from ordinary video cameras [33]. However, using cameras suffers from a critical shortcoming that they could not work properly in poor-lighting environments, which limits the application of this approach in many practical scenarios, e.g., factories with dimmed light and outdoor foggy environments.

### 6.3 RF-based Vibration Monitoring

RF signals have been widely investigated for vibration monitoring due to the battery-free, cost-effective, and light-independent benefits. At first, RFID systems are used to measure the vibration of the target object, which is attached with passive RFID tags [36]. When the object vibrates, the RFID tag moves along with the object. The phase of the signal from the RFID tag involves the vibrating displacement information. However, since the wavelength of RFID signal is in the cm level, it is difficult to accurately extract the tiny vibration pattern in the sub-mm level. Although researchers have investigated amplifying the signal phase for RFID systems, they require multiple (4-6) RFID tags to retrieve the original vibration displacement of a single object [35], bringing much inconvenience for multi-point deployment.

In contrast, the mmWave radar signal with mm-level wavelength has a higher resolution for vibration measurement. Existing works have applied mmWave radars for vibration monitoring [13, 19, 29]. However, they mainly regard the vibrating object as a single point and extract its vibration pattern. In practice, many structures are composed of multiple components which require to be monitored at the same time. Hence, our work dedicatedly realizes multi-point vibration monitoring with a novel design of the vibration marker and advanced methods to accurately estimate the vibration indicators.

## 7 DISCUSSION AND FUTURE WORK

In this section, we discuss some practical issues related to the deployment of Multi-Vib system.

**Resolution of marker detection:** In Multi-Vib, the minimum range and angle between two markers are limited by the radar bandwidth and the number of antennas. The radar we use has a 4GHz bandwidth, which

corresponds to a  $3.75\text{cm}$  resolution. Meanwhile, through our experiments, eight antennas on the radar can achieve around  $10^\circ$  angle resolution. Thus, markers that are within the range and angle resolution cannot be clearly detected. While, in practice, for multi-point vibration monitoring on structures, points actually have a certain distance (e.g.,  $> 10\text{cm}$ ) from each other, because nearby points tend to share a similar vibration pattern. Thus, current range and angle resolutions can properly fulfill the multi-point deployment requirement.

**Multi-dimension and multi-plane vibration measurement:** In Section 2.1, we have shown that the mmWave radar functions as a one-dimension vibration meter. In practice, some applications may demand three-dimension measurements. Our system can be extended to serve this purpose. We can employ three radars in each dimension to transmit and receive signals. Meanwhile, we can concatenate three markers in the same plane with one side overlapping with each other to head towards each dimension.

In this work, we mainly detect vibration points in nearby horizontal planes since the employed commercial radar can only accurately report the azimuth AOA. In practice, we may also require the elevation AOA if vibration points are in distant planes. To achieve this, we can add another radar and vertically rotate it by  $90^\circ$  to measure the elevation AOA. While, multi-dimension and multi-plane vibration measurements require a careful design of the geometry among the radar and markers as well as the signal synchronization among multiple radars. In our future work, we will deal with the above complex vibration measurement scenarios.

**Vibration monitoring under out-of-sight circumstances:** In practice, some target vibration points might be difficult to detect using a single radar. For example, if the radar faces to the front side of the motor, the points on the back side may not be detected because the line-of-sight (LOS) between them and the radar is blocked. Existing works attempt to employ the non-LOS multipath signals to sense the out-of-sight target, which, however, is not applicable for our vibration monitoring scenario. Because the multipath signal is much weaker than the LOS signal, making it difficult to be captured by the mmWave radar. In addition, current mmWave radar's antennas are inherently directional, which fail to monitor points in all directions. To this end, to fully cover the vibration points located at different positions and sides on the structure, we may deploy multiple (i.e., 2-4) mmWave radars to capture the signals reflected from the corresponding vibration points.

## 8 CONCLUSION

In this paper, we present the Multi-Vib system for multi-point vibration monitoring using the commercial mmWave radar. The system provides a cost-effective, passive, and precise approach for monitoring multiple points' vibration simultaneously. The novelty of Multi-Vib lies in designing the marker from the retro-reflective trihedral reflector. With the help of our vibration markers, we can achieve accurate and explicit detection of multiple vibration points. Then, we propose a series of radar signal processing methods, including null steering and antenna array permutation, to denoise the radar signal phase for an accurate estimation of the vibration displacement. Through extensive evaluation experiments, the Multi-Vib system shows high accuracy in vibration frequency and displacement p-p value estimation. In the meantime, our system can be effectively applied to monitor real-world machines and civil structures.

## ACKNOWLEDGMENTS

This work was supported by the Research Institute for Artificial Intelligence of Things, The Hong Kong Polytechnic University, Hong Kong Collaborative Research Fund C5018-20G, Hong Kong RGC Theme-based Research Scheme T22-502/18-R, the National Nature Science Foundation of China under Grant 62102139, the Nature Science Foundation of Hunan Province of China under Grant 2022JJ30168, and the Fundamental Research Funds for the Central Universities under Grant 531118010612.

## REFERENCES

- [1] Tarig Ibrahim Osman Ahmed and Moutaman Mirghani. 2018. Estimation of Radar Cross Sectional Area of Target using Simulation Algorithm. *International Journal of Research Studies in Electrical and Electronics Engineering* 4, 2 (2018).
- [2] Ali Al-Sharadqah and Nikolai Chernov. 2009. Error analysis for circle fitting algorithms. *Electronic Journal of Statistics* 3 (2009), 886–911.
- [3] American Mechanist 2022. The Benefits of Multi-Channel Vibration Measurement. <https://www.americanmachinist.com/shop-operations/article/21897637/the-benefits-of-multichannel-vibration-measurement>.
- [4] Paris Ang and George V Eleftheriades. 2018. A passive redirecting Van Atta-type reflector. *IEEE Antennas and Wireless Propagation Letters* 17, 4 (2018), 689–692.
- [5] Dongyang Ao, Yuanhao Li, Cheng Hu, and Weiming Tian. 2017. Accurate analysis of target characteristic in bistatic SAR images: A dihedral corner reflectors case. *Sensors* 18, 1 (2017), 24.
- [6] AWR1843BOOST 2022. AWR1843BOOST and IWR1843BOOST Single-Chip mmWave Sensing Solution User's Guide. <https://www.ti.com/tool/AWR1843BOOST>.
- [7] Business Standard 2022. Over 13,000 lives lost due to structure collapses in last 5 years. <https://www.business-standard.com/article/current-affairs/over-13-000-lives-lost-due-to-structure-collapses-in-last-5-years-116040200362-1.html>.
- [8] Naval Air Warfare Center. 1997. Electronic warfare and radar systems engineering handbook. *Electronic Warfare Division, Point Mugu, CA* (1997).
- [9] J Geoffrey Chase, NICOLAS H Hudson, Jessica Lin, Rodney Elliot, and Aylwin Sim. 2005. Nonlinear shake table identification and control for near-field earthquake testing. *Journal of Earthquake Engineering* 9, 04 (2005), 461–482.
- [10] Justin Gejune Chen. 2016. *Video camera-based vibration measurement of infrastructure*. Ph.D. Dissertation. Massachusetts Institute of Technology.
- [11] Justin G Chen, Abe Davis, Neal Wadhwa, Frédo Durand, William T Freeman, and Oral Büyüköztürk. 2017. Video camera-based vibration measurement for civil infrastructure applications. *Journal of Infrastructure Systems* 23, 3 (2017), B4016013.
- [12] Nikolai Chernov and Claire Lesort. 2005. Least squares fitting of circles. *Journal of Mathematical Imaging and Vision* 23, 3 (2005), 239–252.
- [13] Gianluca Ciattaglia, Adelmo De Santis, Deivis Disha, Susanna Spinsante, Paolo Castellini, and Ennio Gambi. 2021. Performance Evaluation of Vibrational Measurements through mmWave Automotive Radars. *Remote Sensing* 13, 1 (2021), 98.
- [14] Sudipta Das, Durbadal Mandal, Sakti Prasad Ghoshal, and Rajib Kar. 2016. Generalization of directivity expressions for antenna arrays. *IEEE Transactions on Antennas and Propagation* 65, 2 (2016), 915–919.
- [15] Yuanfeng Duan, Qianyi Chen, Hongmei Zhang, Chung Bang Yun, Sikai Wu, and Qi Zhu. 2019. CNN-based damage identification method of tied-arch bridge using spatial-spectral information. *Smart Struct. Syst., Int. J.* 23, 5 (2019), 507–520.
- [16] Stephan Ebersbach and Zhongxiao Peng. 2008. Expert system development for vibration analysis in machine condition monitoring. *Expert systems with applications* 34, 1 (2008), 291–299.
- [17] Efficient Plant 2022. Three- And Four-Channel Vibration Data Collection. <https://www.efficientplantmag.com/2009/07/three-and-four-channel-vibration-data-collection/>.
- [18] Junchen Guo, Yuan He, Chengkun Jiang, Meng Jin, Shuai Li, Jia Zhang, Rui Xi, and Yunhao Liu. 2021. Measuring Micrometer-Level Vibrations with mmWave Radar. *IEEE Transactions on Mobile Computing* (2021).
- [19] Chengkun Jiang, Junchen Guo, Yuan He, Meng Jin, Shuai Li, and Yunhao Liu. 2020. mmVib: micrometer-level vibration measurement with mmwave radar. In *Proceedings of the 26th Annual International Conference on Mobile Computing and Networking*. 1–13.
- [20] Alan L Kachelmyer and Kenneth Schultz. 1995. Laser vibration sensing. (1995).
- [21] Kiyoyuki Kaito, Masato Abe, and Yozo Fujino. 2005. Development of non-contact scanning vibration measurement system for real-scale structures. *Structure and Infrastructure Engineering* 1, 3 (2005), 189–205.
- [22] Jyrki Kullaa. 2010. Vibration-based structural health monitoring under variable environmental or operational conditions. In *New trends in vibration based structural health monitoring*. Springer, 107–181.
- [23] Ping Li, Zhenlin An, Lei Yang, Panlong Yang, and QiongZheng Lin. 2019. RFID harmonic for vibration sensing. *IEEE Transactions on Mobile Computing* 20, 4 (2019), 1614–1626.
- [24] Zhao-feng Lu, Min Qin, He Chen, Li Lin, and Ying Zhang. 2007. Application and Investigation of Piezoelectric Accelerometer on Vibration Measurement System. *Instrument Technique and Sensor* 7 (2007), 3–4.
- [25] SKF Condition Monitoring. 1994. Vibration diagnostic guide.
- [26] SA Neild, PD McFadden, and MS Williams. 2003. A review of time-frequency methods for structural vibration analysis. *Engineering Structures* 25, 6 (2003), 713–728.
- [27] Sandeep Rao. 2017. Introduction to mmWave sensing: FMCW radars. *Texas Instruments (TI) mmWave Training Series* (2017).
- [28] Alessandro Sabato, Christopher Nierzrecki, and Giancarlo Fortino. 2016. Wireless MEMS-based accelerometer sensor boards for structural vibration monitoring: a review. *IEEE Sensors Journal* 17, 2 (2016), 226–235.

- [29] Martin L Smith, John A Scales, Manoja Weiss, and Brian Zadler. 2010. A low-cost millimeter wave interferometer for remote vibration sensing. *Journal of Applied Physics* 108, 2 (2010), 024902.
- [30] Gabriel Taubin, Fernando Cukierman, Steve Sullivan, Jean Ponce, and David J. Kriegman. 1994. Parameterized families of polynomials for bounded algebraic curve and surface fitting. *IEEE Transactions on Pattern Analysis and Machine Intelligence* 16, 3 (1994), 287–303.
- [31] UpKeep 2022. Predictive and Preventive Maintenance Statistics. <https://www.upkeep.com/learning/maintenance-metrics/maintenance-statistics>.
- [32] H Van Trees. 2002. Planar Arrays and Apertures. *Optimum Array Processing* (2002), 231–331.
- [33] Neal Wadhwa, Michael Rubinstein, Frédéric Durand, and William T Freeman. 2013. Phase-based video motion processing. *ACM Transactions on Graphics* 32, 4 (2013), 1–10.
- [34] Christine E Wittich and Tara C Hutchinson. 2015. Shake table tests of stiff, unattached, asymmetric structures. *Earthquake Engineering & Structural Dynamics* 44, 14 (2015), 2425–2443.
- [35] Binbin Xie, Jie Xiong, Xiaojiang Chen, and Dingyi Fang. 2020. Exploring commodity RFID for contactless sub-millimeter vibration sensing. In *Proceedings of the 18th Conference on Embedded Networked Sensor Systems*. 15–27.
- [36] Lei Yang, Yao Li, Qiongzhen Lin, Huanyu Jia, Xiang-Yang Li, and Yunhao Liu. 2017. Tagbeat: Sensing mechanical vibration period with cots rfid systems. *IEEE/ACM transactions on networking* 25, 6 (2017), 3823–3835.

## A CALCULATING THE NEW STEERING VECTOR FOR NULL STEERING

In this appendix, we derive the solution for the optimization problem in Eq. (6), with one and two interfering markers in the same range bin as representative examples. One can acquire the solution for more number of interfering markers following the same solution idea.

For one interfering marker with AOA of  $\phi_{n_1}$ , we first formulate a function  $f(w_d, w_d^H)$  by combining the objective function and constrain using a Lagrange multiplier constraint variable  $\gamma$  as follows<sup>1</sup>:

$$\begin{aligned} f(w_d, w_d^H) &= [w_d - w(\phi_t)]^H \cdot [w_d - w(\phi_t)] + 2\text{Re}\{w_d^H \cdot w(\phi_{n_1}) \cdot \gamma\} \\ &= [w_d - w(\phi_t)]^H \cdot [w_d - w(\phi_t)] + w_d^H \cdot w(\phi_{n_1}) \cdot \gamma + w(\phi_{n_1})^H \cdot w_d \cdot \gamma^* \end{aligned} \quad (10)$$

Then, we take the gradient of  $f(w_d, w_d^H)$  with respect to  $w_d^H$  and set it to zero, i.e.,  $\nabla_{w_d^H} f = 0$ . Note that  $w_d^H$  and  $w_d$  are independent when taking the gradient.

$$\begin{aligned} \nabla_{w_d^H} f &= w_d - w(\phi_t) + w(\phi_{n_1}) \cdot \gamma = 0 \\ \therefore w_d &= w(\phi_t) - \gamma \cdot w(\phi_{n_1}) \end{aligned} \quad (11)$$

Taking the above result of  $w_d$  into the constraint  $w_d^H \cdot w(\phi_{n_1}) = 0$ , we can get equations as below:

$$\begin{aligned} [w(\phi_t) - \gamma \cdot w(\phi_{n_1})]^H \cdot w(\phi_{n_1}) &= 0 \\ [w(\phi_t)^H - \gamma^* \cdot w(\phi_{n_1})^H] \cdot w(\phi_{n_1}) &= 0 \\ w(\phi_t)^H \cdot w(\phi_{n_1}) &= \gamma^* \cdot w(\phi_{n_1})^H \cdot w(\phi_{n_1}) \\ \gamma &= \frac{w(\phi_{n_1})^H \cdot w(\phi_t)}{w(\phi_{n_1})^H \cdot w(\phi_{n_1})} \end{aligned} \quad (12)$$

Finally, by applying  $\gamma$  into  $w_d = w(\phi_t) - \gamma \cdot w(\phi_{n_1})$ , we can obtain:

$$w_d = w(\phi_t) - \frac{w(\phi_{n_1}) \cdot w(\phi_{n_1})^H}{w(\phi_{n_1})^H \cdot w(\phi_{n_1})} \cdot w(\phi_t) \quad (13)$$

Similarly, for two interfering markers with AOA of  $\phi_{n_1}$  and  $\phi_{n_2}$ , respectively,  $f(w_d, w_d^H)$  is formulated with two Lagrange multiplier constraint variables  $\gamma$  and  $\epsilon$  as follows:

$$f(w_d, w_d^H) = [w_d - w(\phi_t)]^H \cdot [w_d - w(\phi_t)] + 2\text{Re}\{w_d^H \cdot w(\phi_{n_1}) \cdot \gamma\} + 2\text{Re}\{w_d^H \cdot w(\phi_{n_2}) \cdot \epsilon\} \quad (14)$$

---

<sup>1</sup>The variable  $\gamma$  can be a complex number, thus we take the real part of  $w_d^H \cdot w(\phi_{n_1}) \cdot \gamma$ .

Accordingly, the gradient of  $f(w_d, w_d^H)$  with respect to  $w_d^H$  is:

$$\begin{aligned}\nabla_{w_d^H} f &= w_d - w(\phi_t) + w(\phi_{n_1}) \cdot \gamma + w(\phi_{n_2}) \cdot \epsilon = 0 \\ \therefore w_d &= w(\phi_t) - \gamma \cdot w(\phi_{n_1}) - \epsilon \cdot w(\phi_{n_2})\end{aligned}\quad (15)$$

Then,  $w_d$  is substituted into the two constraints  $w_d^H \cdot w(\phi_{n_1}) = 0$  and  $w_d^H \cdot w(\phi_{n_2}) = 0$ , from which we can obtain the expression of  $\gamma$  and  $\epsilon$  as:

$$\gamma = \frac{w(\phi_{n_2})^H \cdot (1 - A)^H \cdot w(\phi_t)}{w(\phi_{n_2})^H \cdot (1 - A) \cdot w(\phi_{n_2})}, \quad \epsilon = \frac{w(\phi_{n_2})^H \cdot (1 - B)^H \cdot w(\phi_t)}{w(\phi_{n_2})^H \cdot (1 - B) \cdot w(\phi_{n_2})}, \quad (16)$$

where  $A = \frac{w(\phi_{n_1}) \cdot w(\phi_{n_2})^H}{w(\phi_{n_2})^H \cdot w(\phi_{n_1})}$ ,  $B = \frac{w(\phi_{n_1}) \cdot w(\phi_{n_1})^H}{w(\phi_{n_1})^H \cdot w(\phi_{n_1})}$ . Finally, with  $\gamma$  and  $\epsilon$  acquired, we can calculate  $w_d$  as:

$$w_d = w(\phi_t) - \frac{w(\phi_{n_2})^H \cdot (1 - A)^H \cdot w(\phi_t)}{w(\phi_{n_2})^H \cdot (1 - A) \cdot w(\phi_{n_2})} \cdot w(\phi_{n_1}) - \frac{w(\phi_{n_2})^H \cdot (1 - B)^H \cdot w(\phi_t)}{w(\phi_{n_2})^H \cdot (1 - B) \cdot w(\phi_{n_2})} \cdot w(\phi_{n_2}) \quad (17)$$

Theoretically, we can import more Lagrange multiplier variables for more number of markers in the same range bin. While in practice, the common cases mainly involve 1-3 markers in a single bin. Thus, the solutions to one and two interfering markers can tackle most of cases.